An Engineering Approach to Blade Designs for Low to Medium Pressure Rise Rotor-Only Axial Fans

R. J. Downie
M. C. Thompson
R. A. Wallis
CSIRO Division of Building, Construction and Engineering, Highett, Victoria, Australia

■ Low to medium pressure rise axial fan equipment of the arbitrary vortex flow rotor-only type is widely used in industrial and commercial applications, with many of the installations and rotor designs being far from optimum. Complex computational methods exist for analyzing flows in, for example, high-speed axial flow compressors with multistage blade rows; however, the designers and manufacturers of low-speed, general-purpose axial flow fan equipment have been reluctant to embrace this technology. A simpler yet reliable design technique is presented that allows this category of ducted axial fan rotors, in the presence of swirl-free inlet flow, to be designed to achieve a specified duty with sufficient accuracy for engineering purposes. Practical blade design recommendations and limits, similar to those that exist for free vortex flow axial rotors, have been established for the arbitrary vortex flow rotor-only case.

The technique employs a straightforward engineering approach to arbitrary vortex flow axial fan rotor design, and the equation set can be solved by using relatively simple numerical methods. Estimates of pressure rise and shaft power characteristics for a proposed fan/rotor design can be computed and the design loop iterated until an acceptable set of blade parameters is identified. It is also possible to analyze the performance of an existing axial fan installation as a prelude to the design of a more efficient and effective replacement rotor.

Experimental data used in validating the design and analysis techniques are also presented. These data include comprehensive Cobra pressure probe surveys of local flow parameters downstream of three different low boss ratio, low solidity, arbitrary vortex flow rotors (all with circular arc camber line type blades) as well as fan performance characteristics for one of the experimental rotors configured as a direct-exhaust fan unit. Installation-dependent factors such as direct-exhaust losses and tip clearance effects are also examined. The analytical technique is shown to provide acceptable estimates of fan/rotor pressure rise performance and shaft power characteristics over a moderately wide range of blade angles and operating conditions.

Keywords: *axial fan design, arbitrary vortex flow, Cobra pressure probe, fan testing, rotor tip clearance*

INTRODUCTION

Axial fan equipment of both the free vortex flow and arbitrary vortex flow types are widely used in industrial and commercial applications. A free vortex flow rotor is designed for swirl-free inlet flow conditions with the local total pressure rise and axial velocity components downstream of the rotor remaining constant across the blade span. As radial flow components are absent, the local swirl or tangential velocity component downstream of the rotor blade elements can be related readily to the total pressure rise through the blade row, and the velocity field is clearly defined. Efficient free vortex flow axial fan designs can be achieved using an existing simplified design technique [1].

An arbitrary vortex flow rotor represents the more general case where the rotor is again designed to accept swirl-free flow at inlet but the local total pressure rise and axial velocity component downstream of the rotor both vary with spanwise position. In this case significant radial flow components exist and the situation is considerably

Address correspondence to Ms. Cathy Bowditch, CSIRO Division of Building, Construction and Engineering, P.O. Box 56, Highett, Victoria 3190, Australia.

Experimental Thermal and Fluid Science 1993; 6:376–401

0894-1777/93/$6.00

more complex. These rotors are primarily used in low to medium pressure rise axial fan equipment of the rotor-only type. These rotor designs and installations are often the result of ad hoc development and are frequently of a poor standard.

In the arbitrary vortex flow case, the balance between the centrifugal force (associated with the tangential or swirl velocity component) and the radial static pressure gradient is achieved by some radial movement of fluid from one parallel elemental annulus to an adjacent one. Therefore, it is important to have a relationship that enables the degree of radial movement to be estimated, thus permitting the downstream velocity field to be established adequately for design purposes.

Kahane [2] employed a radial equilibrium equation and assumed, for design purposes, that the radial velocity component terms could be ignored. This allowed a determination of spanwise downstream axial velocity components that would satisfy the equilibrium condition. Kahane demonstrated experimentally the validity of this design approach for two axial rotors, both with boss ratio $x_b = 0.69$. One rotor was designed to give a nearly constant spanwise downstream tangential velocity distribution, while the other rotor was designed to achieve a nearly linear increase in the spanwise downstream tangential velocity with radius (solid-body rotation), which coincided with zero blade twist.

Wallis [3] developed Kahane's design equations and was able to propose a more general treatment for the design of ducted arbitrary vortex flow rotor-only axial fans. This design procedure depended solely on Kahane's experimental success; Wallis [1] subsequently recommended caution pending further experimental validation. More complex computational methods have been proposed for analyzing the flow through turbomachinery, including high-speed axial flow compressors with multistage blade rows, where large axial, radial, and tangential pressure gradients exist [4]. However, the designers and manufacturers of low-speed, general-purpose axial flow fan equipment have been reluctant to embrace this technology, and the development of a simple yet reliable engineering technique for designing efficient arbitrary vortex flow axial fan rotors continues to be seen as a practical requirement by these fan manufacturers and industrial users alike.

The CSIRO Division of Building, Construction and Engineering has further developed the Kahane-Wallis design method, enabling arbitrary vortex flow rotor-only axial fans to now be designed with an acceptable degree of accuracy for engineering purposes. An experimental program that validates the design method for small boss ratios ($x_b \approx 0.4$) was undertaken using three experimental 610 mm diameter axial rotors of differing blade geometries but nearly identical design duty capability. This duty is consistent with that for fan-cooled heat exchanger assemblies.

Spanwise distributions of velocity and pressure downstream of each of the experimental rotors were comprehensively surveyed in a specially instrumented test rig. One of the rotors was also tested in a direct-exhaust fan assembly [5] as further validation of the design and analysis method. Direct-exhaust losses and rotor tip clearance effects were also addressed in the test program.

The following sections of this paper deal with the arbitrary vortex flow design philosophy and method, the experimental program used to validate the design and analysis methodology, and the important conclusions that follow from this work. The section dealing with the experimental apparatus and test procedures need not be read in depth unless the material is of specific interest to the reader.

The terminology used throughout this paper is generally consistent with that of Refs. 1, 3, and 6. Figure 1 depicts some of the more important features of cambered plate and airfoil section blade elements.

ARBITRARY VORTEX FLOW DESIGN PHILOSOPHY

Arbitrary vortex flow axial fan rotor design procedures provide a practical tool when any of the following constraints and conditions apply:

1. The blade root chord length must be constrained to ensure that blade overlap does not occur when the rotor is to be injection-molded in one piece.
2. A large nondimensional total pressure rise is to be achieved in the absence of stator vanes and/or a diffuser assembly, and thus a small rotor boss diameter must be used to minimize downstream mixing losses and maximize through-flow.
3. An existing free vortex flow rotor is to be replaced and

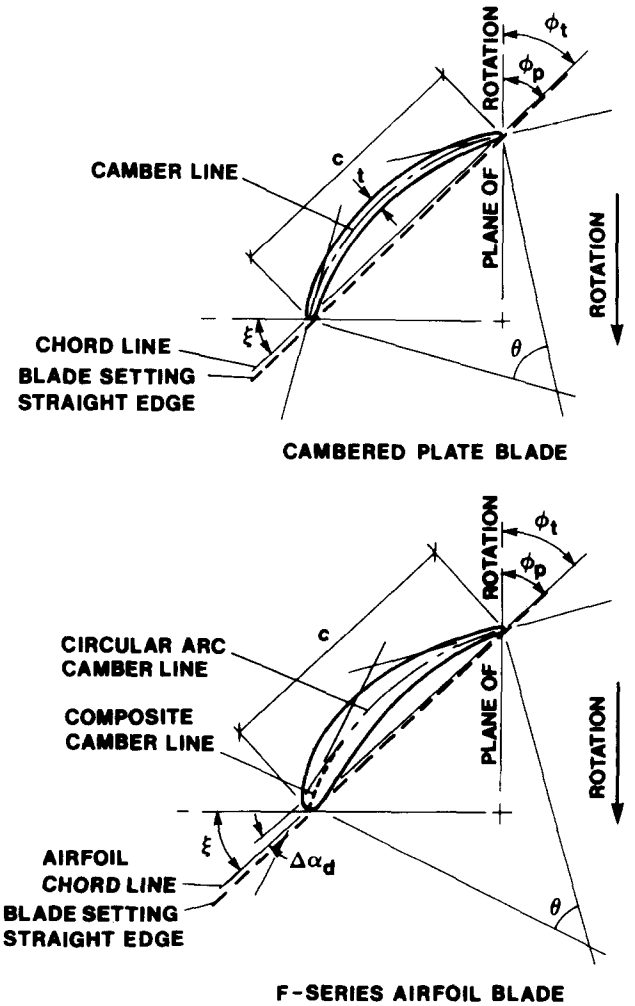

Figure 1. Fan blade element terminology.

an increase in mean total pressure rise capability is required through rotor blade redesign alone.

In an axial fan rotor, the local blade speed increases linearly with radius, and hence the pressure rise capability of the inboard portion of the blade becomes a limiting factor, especially in the case of a free vortex flow rotor design. However, arbitrary vortex flow designs normally result in the local total pressure rise increasing toward the blade tip, and consequently the design mean total pressure rise across the rotor can be higher than for a corresponding free vortex flow design of equal inboard pressure rise. The magnitude of the blade root loading in an arbitrary vortex flow design is controlled by limiting the total twist between the tip and the root of the blade.

ARBITRARY VORTEX FLOW ROTOR DESIGN METHOD

The design method proposed by Wallis [1] assumed in part that the total pressure rise at the blade midspan element was representative of the mean rotor behavior and that the spanwise swirl velocity components could be approximated by a linear distribution. The current procedure instead allows a piecewise linear representation of the swirl distribution to be used, and the mean rotor performance is estimated by applying a mass-weighted integration procedure to the spanwise pressure distributions. The revised design equation set developed in the Appendix includes first-order terms associated with the radial redistribution of flow through the rotor.

The method, as applied to new rotor design, employs a straightforward approach incorporating appropriate blade design guidelines to establish an efficient and practical rotor design capable of achieving the main design duty requirement. In the event that the performance specification also calls for off-design duties to be met, then fan pressure rise and shaft power characteristics for the proposed rotor design are calculated and the design loop is then iterated until an acceptable set of rotor/blade parameters is identified. Similarly, an existing axial fan installation of the rotor-only type may in many cases be analyzed to provide estimates of the fan pressure rise and shaft power characteristics.

Design of New Arbitrary Vortex Flow Rotors

Rotor design involves identifying a suitable combination of blade camber θ, stagger angle ξ, and blade solidity σ distributions that will enable the fan rotor to achieve a specified volume flow rate and rotor pressure rise.

For axial rotor design purposes, the fan volume flow rate can be converted to a rotor nondimensional tip flow coefficient Λ [1], where

$$\Lambda = \bar{V}_a/\Omega R$$

and the total pressure rise can be converted to a nondimensional pressure rise coefficient K [1], which is typically defined by

$$K = \Delta H/\left[(1/2)\rho \bar{V}_a^2\right]$$

In the case of spanwise distributions, the blade element position can be specified in terms of a nondimensional radius ratio x [1], which is defined as the ratio of the blade element radius to the fan duct radius.

The following design procedures are for arbitrary vortex flow rotor-only units with circular arc camber line blading, and the design recommendations and limits are primarily intended for low boss ratio fans with demanding nondimensional pressure rise duty requirements. Appropriate design recommendations for higher boss ratio arbitrary vortex flow designs will tend to approach those currently used for free vortex flow axial rotor designs [1]. The degree of iteration necessary to effect a satisfactory arbitrary vortex flow rotor design solution will depend upon the experience of the designer.

The design technique for arbitrary vortex flow rotors is as follows.

Step 1 Preliminary estimates are made of the fan overall efficiency η_T or η_E (including fan/rotor configuration-dependent losses such as the effects of excess rotor tip clearance), the fan/hub diameters, and the rotor shaft speed. This allows the specified fan duty requirement to be converted to a nondimensional tip flow coefficient Λ and a theoretical mean total pressure rise coefficient K_{th}.

Step 2 Initially it is assumed that the local total pressure rise coefficient k_{th} at the blade midspan position is approximately equal to K_{th}, and a first estimate of the local swirl coefficient ϵ_s at the blade midspan position is then obtained using Eq. (A.33) (see Appendix). The tentatively recommended maximum design values for ϵ_s at the blade midspan position range from 0.7 for $x_b = 0.4$ to 0.85 for $x_b = 0.7$. The preliminary estimates of fan/hub diameter and shaft speed (step 1 above) may need to be modified to satisfy this design recommendation.

Step 3 A trial spanwise swirl coefficient distribution (usually linear or near-linear) through the previously calculated ϵ_s midspan value and a preliminary estimate for the rotor blade efficiency η_{Rb} (say 85%) are selected. In the case of a linear swirl distribution, the required gradient changes progressively from a negative to a positive value as x_b is increased and typically may range between -0.8 and $+1.0$ depending on the values of x_b and K_{th}. The corresponding spanwise downstream axial velocity ratio distribution Σ_a is then calculated using equations (A.55) and (A.56). The calculated axial velocity ratio at the blade root should exceed a tentatively suggested design limit of 0.4 for small boss ratio rotors. This limiting value will increase in magnitude with x_b owing to blade design problems. The trend toward more positive gradients of the swirl distribution will eventually result in these limits being exceeded.

Step 4 The trial spanwise distribution of swirl coefficient and the corresponding spanwise values of downstream axial velocity ratio are used in conjunction with Eqs. (A.13), (A.14a), (A.14b), and (A.27) to produce a tentative estimate of the blade loading factor $C_L\sigma$ spanwise requirements. The drag-related term in Eq. (A.27) is usually small, and for convenience it can be ignored in the first instance. However, this drag-related term affords a necessary correction and should be considered in the later design iterations.

Step 5 Spanwise distributions of lift coefficient C_L and solidity σ that satisfy the above blade loading needs are then established by iterative means.

If the blade loading factor at the root approaches 1.2, then it is recommended that the root solidity be selected such that the corresponding blade element isolated lift coefficient C_{L_i} requirement is kept below 1.3. Lift coefficients of this magnitude are usually associated with blade element camber angles approaching 36°. High solidity in the blade root region will cause interference effects between neighboring blades and necessitates the use of an interference factor C_L/C_{L_i}, which is discussed further in the Appendix. In this case the corresponding isolated lift coefficient C_{L_i} requirement at the blade root will be higher than the calculated C_L design value.

The spanwise distribution of solidity is then selected by iteration, adopting either a constant or tapered chord blade form. For equally spaced blades it can be shown that the ratio nc/R is equal to $2\pi x\sigma$. The value of these terms is constant in the case of constant-chord blades, whereas both the chord c and the ratio nc/R will vary linearly with radius ratio x for a straight tapered blade. The blade tip solidity is set such that the corresponding lift coefficient requirement in the blade tip region is conservative. For small boss ratio rotors, blade tip lift coefficients below approximately 0.7 are recommended and are usually associated with blade element camber angles of approximately 18–25°. This approach is important if an acceptable increment in peak total pressure rise performance is to be achieved after the onset of flow separation from the blade root.

The number of blades and the blade chord details are selected with strength and manufacturing considerations in mind. A blade aspect ratio l/c of approximately 2 is seen as desirable to promote good blade stiffness.

Step 6 The isolated lift coefficient requirements are then evaluated against available two-dimensional airfoil lift and drag data such as those referred to in the Appendix. An airfoil's lift and drag performance can be significantly affected by Reynolds number and blade surface irregularities [1, 7, 8]. Some design guidance is available in Ref. 1.

Appropriate cambered plate or airfoil sections are chosen across the blade span, and the corresponding incidence angle α and stagger angle ξ are calculated such that the required lift force requirements are satisfied. The blade section camber should be chosen with care to minimize the corresponding profile drag losses, taking into consideration any rotor off-design operational requirements. The camber value chosen for the blade root should enable the required isolated lift coefficient to be achieved while also allowing a prudent margin with respect to the maximum attainable section lift coefficient. The spanwise distribution of camber usually takes the form of a smooth curved line of decreasing slope toward the blade tip.

Step 7 The blade element drag coefficients are obtained by combining the appropriate estimates of profile drag C_{D_p} with a secondary drag loss C_{D_s}, the latter being based on the blade midspan position. The empirical relationship given in Eq. (A.38) provides a useful estimate of C_{D_s} in a well-designed axial fan rotor.

Step 8 The spanwise distributions of theoretical total pressure rise coefficient k_{th}, blade element pressure loss coefficient k_R, actual total pressure rise coefficient k_r, and blade element efficiency η_{Rb} across the rotor are calculated using Eqs. (A.33), (A.44), (A.45), and (A.46), respectively. The corresponding static pressure rise coefficient distribution can be obtained using Eq. (A.35). An integration procedure using a mass-weighted technique suitable for incompressible flows [9] can be applied to the above spanwise pressure distributions to calculate the rotor mean theoretical and actual total pressure rise coefficients. Hence the rotor mean total pressure rise estimates, ΔH_{th} and ΔH_r, corresponding to a zero-loss rotor tip clearance situation can be calculated.

Step 9 These total pressure rise estimates, together with the volume flow rate, enable the shaft input power W and the overall total efficiency η_R to be calculated for a zero-loss rotor tip clearance situation. The downstream axial and tangential flow velocity pressure component distributions can also be integrated [9] to enable the fan inlet total pressure (FITP) and the rotor exhaust efficiency η_E to be estimated for a zero-loss rotor tip clearance situation. The relevant total pressure rise and shaft power are then corrected for other specific configuration losses, for example, those due to rotor tip clearance effects. The influence of excess tip clearance is discussed in Ref. 1, and further information pertaining to suggested corrections for low to medium boss ratio direct-exhaust applications is given in the Appendix.

Step 10 The whole or part of the design process should be iterated until the designer has identified a practical rotor design that meets the specified duty condition. Spanwise distributions of blade geometry parameters such as chord, camber, and stagger angle are usually smooth and faired in the final design. The predicted blade setting angle ϕ_i is the complementary angle to the stagger angle ξ at a specified blade span position.

In the design method it has been assumed that

1. The redistribution of tangential (swirl) and axial velocity components are both essentially complete immediately downstream of the rotor blading.
2. The contribution from the local downstream radial velocity components in the calculations represents a second-order effect and as such can be ignored.
3. The arithmetic mean of the upstream and downstream axial velocity components at a given radius can be used to modify the local flow and swirl coefficients for the purpose of blade element design.

In the event that the motor is required to operate over a wide range of pressure duties and/or a maximum available shaft input power has been specified, then the designer would use the following procedure to analyze the off-design performance of the proposed rotor design.

Analyzing Arbitrary Vortex Flow Rotor Designs

It may be possible to analyze the performance of either a proposed or an existing arbitrary vortex flow rotor-only

fan assembly, given the rotor blade geometry (chord, camber, and stagger angle distributions), the relevant two-dimensional lift and drag force data, the fan/hub diameters, the rotor tip clearance, and the shaft rotational speed. The equation set given in the Appendix is used in conjunction with the following procedure to provide estimates of fan pressure rise and shaft power over the range of nominated flow rate conditions, provided that the distributions of swirl coefficient result in positive axial velocity components over the blade span at these flow rates.

An algorithm for analyzing an arbitrary vortex flow rotor design is as follows.

1. Make first estimates of the rotor total efficiency η_R and theoretical mean total pressure rise coefficient K_{th}. Equating K_{th} to the local total pressure rise coefficient k_{th} at the blade midspan and using Eq. (A.33), tentatively establish the local swirl coefficient ϵ_s at the blade midspan.
2. Assume initially that the spanwise local swirl coefficients are constant at the value estimated above.
3. Compute the corresponding downstream axial velocity ratio distribution that satisfies Eqs. (A.55) and (A.56). The first equation explicitly gives the downstream axial velocity ratio provided x_0 (the position where the downstream and upstream axial velocity components are equal) is known. The value of x_0 can be iteratively adjusted until Eq. (A.56) is satisfied to some desired precision. This procedure can be automated by using a standard root-finding technique such as the false-position method or half-interval search [10].
4. Calculate the implied spanwise values of the angle of incidence using the relationship $\alpha = \beta_m - \xi$, where β_m values are calculated using Eqs. (A.13), (A.14a), and (A.14b).
5. Estimate by iteration the secondary drag based on the midspan blade element position using Eqs. (A.13), (A.26), and (A.38).
6. Given the relevant lift and drag force data (in terms of blade camber, angle of incidence, and blade Reynolds number, similar to those given in the Appendix) and using an approximate relationship between solidity, stagger angle, and the lift coefficient modification due to multiplane interference (see Appendix), establish a lift coefficient distribution for the angle of incidence values calculated in step 4. A second estimate of the lift coefficient distribution can be obtained from Eq. (A.26) using iteration, the β_m values from Eq. (A.13), and the secondary drag estimate from step 5. The difference between the two lift coefficient distributions is then quantified by calculating a weighted "least squares error" over the blade span. In this case it was decided to use a root mean square technique, with the square of the difference between the two lift coefficients estimates for each blade element being weighted according to the blade element radius ratio.
7. If the least squares error is not a minimum, then adjust the swirl distribution, return to step 2, and continue iterating. This outer iteration loop can be automated by employing methods for minimizing multidimensional functions such as Powell's method [10].
8. Once the best-fit swirl distribution has been determined, estimate the rotor theoretical total pressure rise and rotor pressure loss coefficient distributions using Eqs. (A.33) and (A.44), respectively. Then apply the integration procedure using the mass-weighted technique for incompressible flow situations [9] to the above spanwise pressure distributions to predict the rotor mean theoretical and actual total pressure rise coefficients and hence the rotor total efficiency corresponding to a zero-loss rotor tip clearance situation.
9. If the estimates of rotor total efficiency (used in step 3 and calculated at step 8) have not converged, then assume the latter to be the best trial estimate to date and return to step 2.
10. Deduce the fan/rotor overall performance by estimating any additional fan configuration-dependent losses (rotor tip clearance effects, etc.) and applying these corrections to the fan pressure rise and efficiency estimates.
11. The above steps 1–10 can then be repeated over a nominated range of flow conditions to predict the approximate fan/rotor pressure rise and shaft power characteristics. Use the previous estimate of swirl coefficient distribution and rotor total efficiency as the initial trial estimate for each new volume flow rate condition.

The estimated fan/rotor pressure rise and shaft power characteristics over the nominated range of flow rate conditions can provide useful information when preparing a fan/rotor performance upgrade specification. If an existing rotor design is to be modified, then the performance benefits derived from intuitive changes to the rotor geometry, such as changes in blade pitch, the number of blades, etc., can be investigated using the above procedure. However, if a completely new rotor design is sought, then the procedure outlined for designing a new rotor would be more appropriate.

EXPERIMENTAL ROTOR DESIGNS FOR VALIDATION PURPOSES

All three rotors, Mark 1, 2, and 3 (Fig. 2), feature adjustable pitch blading and are of aluminum construction, with the latter two having cast blades. The Mark 1 rotor has eight constant-thickness (t = 2 mm), circular arc camber line blades and, except for the blade root region (inboard of radius ratio x = 0.5), employs conventional blade design and loading limitations as applied in free vortex flow fan design practice [1]. The rotor features a continuously varying blade chord (84 mm at the tip increasing to 135 mm at the root) and displays blade overlap in the blade root region.

The Mark 2 and 3 rotors employ significant design modifications from the Mark 1 rotor, including the adoption of constant-chord (125 mm) blades. The blade chord departures away from the Mark 1 design result from a desire to reduce the root solidity, eliminating any overlap at the blade root, and to increase the tip solidity in recognition of a tendency of arbitrary vortex flow fans to stall from the blade tip region. The former is a requirement if the rotor is to be plastic injection-molded in one piece.

The Mark 2 rotor uses six circular arc camber line lamina blades (t = 4 mm, faired to 2 mm in thickness over the final 20% blade chord length), whereas the Mark 3 rotor is fitted with six F-series airfoil blades of 10%

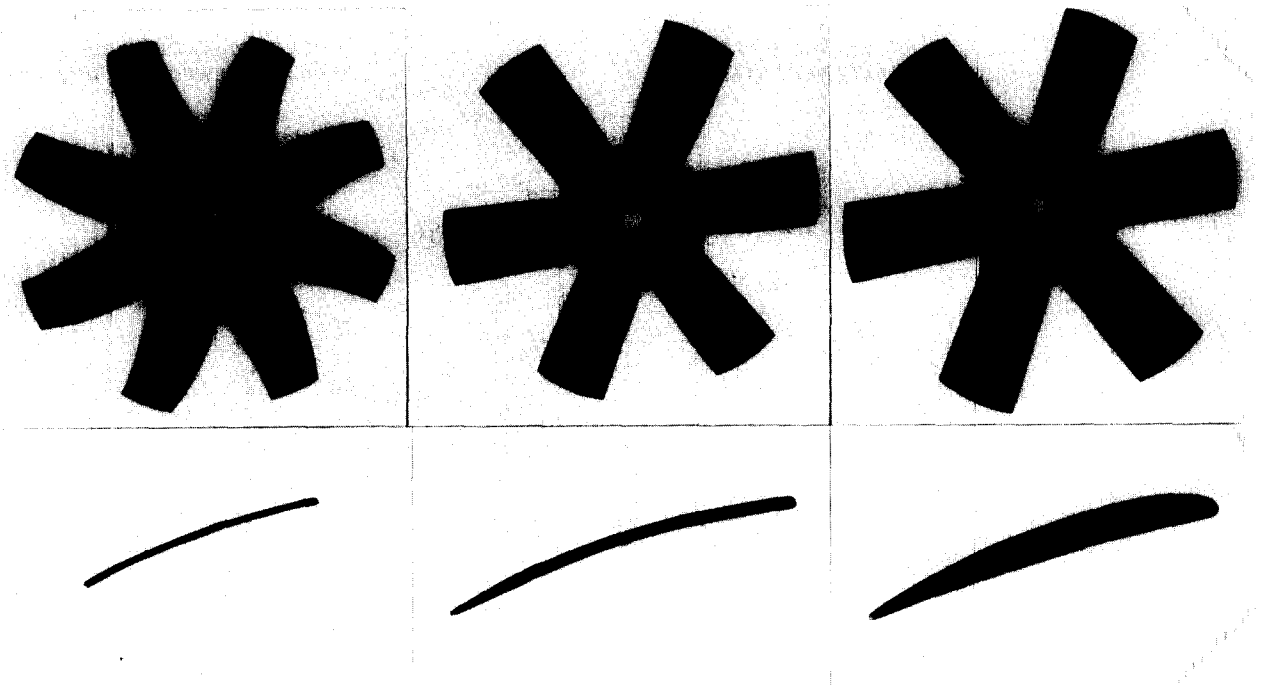

Figure 2. Test rotors with respective blade tip cross-sectional profiles. From left to right: Mark 1, eight cambered plate blades; Mark 2, six cambered plate blades; Mark 3, six F-series airfoil blades.

maximum thickness and featuring $d = 2.5\%$ "nose droop" [1, 6]. It was postulated that the reduction in inboard solidity in these latter two rotors would alleviate multiplane interference effects between neighboring blades and allow higher overall lift coefficients to be achieved in the blade root region. The inboard blade element cambers are therefore slightly greater than for the Mark 1 blading.

EXPERIMENTAL APPARATUS AND PROCEDURES

An arbitrary vortex flow fan rotor test rig (Fig. 3) was commissioned to enable detailed spanwise blade performance measurements (outside of the wall boundary layer regions) to be conducted on the three 610 mm diameter (boss ratio $x_b = 0.38$) experimental axial fan rotors. An existing fan inlet chamber assembly test facility (Fig. 4) was used to measure the overall performance characteristics of several fan/rotor configurations.

Arbitrary Vortex Flow Rotor Test Rig

An aerodynamic outline of the arbitrary vortex flow fan test rig is shown in Fig. 3. The test fan draws laboratory air through six permeable walls of a screen box (*1*) into a British Standard (BS) conical inlet [11] flow rate measuring module (*2*). The air then passes through an inlet flow conditioning module (*3*), which incorporates a screen/honeycomb configuration as recommended in Ref. 12, and into a machined fan inlet duct (*4*). A flow visualization module (*5*) incorporating a curved acrylic window can be fitted between the fan inlet duct and a machined fan tube (*6*) as required. The air enters the fan tube module, where it passes through the test rotor, which imparts a swirling motion to the flow, the latter being a function of the fan loading. From the fan annulus the flow enters an expanding annular diffuser (*7*) prior to being discharged to the laboratory through an adjustable loading screen system (*8*).

The rotor drive system is fully enclosed in a centerbody and supported by three pairs of faired struts in the fan tube and annular diffuser. A three-phase electric motor (*9*) is electrically connected via a static frequency converter speed control unit. An inline shaft torque transducer assembly (*10*) and a shaft rotational speed module (*11*) are housed within the expanding centerbody section and the cylindrical centerbody section behind the test rotor (*12*), respectively.

The fan pressure loading is altered by initially adjusting the loading screen assembly (*8*) axially with respect to the diffuser outlet as required. A movable perforated screen can be slid across the face of a similar stationary screen, enabling the open area of the loading screens to be varied. Locating the loading screen assembly downstream of the test rotor ensures that the turbulence level upstream of the rotor blading is independent of the fan pressure loading.

Static pressure measuring stations (*13*) consisting of sets of four wall tappings spaced 90° apart around the duct circumference are located on the conical inlet (*2*), on the machined aluminum fan inlet duct (*4*), and in the fan annulus (*6*) on the machined aluminum fan tube and corresponding sheet metal centerbody (Fig. 3). Seven Cobra pressure probe (*14*) mounting stations are available: I, II, III, and IV on the fan inlet duct (*4*) and V, VI, and VII along the fan tube (*6*) downstream of the blading.

Fan Inlet Chamber Assembly Test Facility

The fan inlet chamber assembly arrangement, used to measure the overall rotor performance for a series of

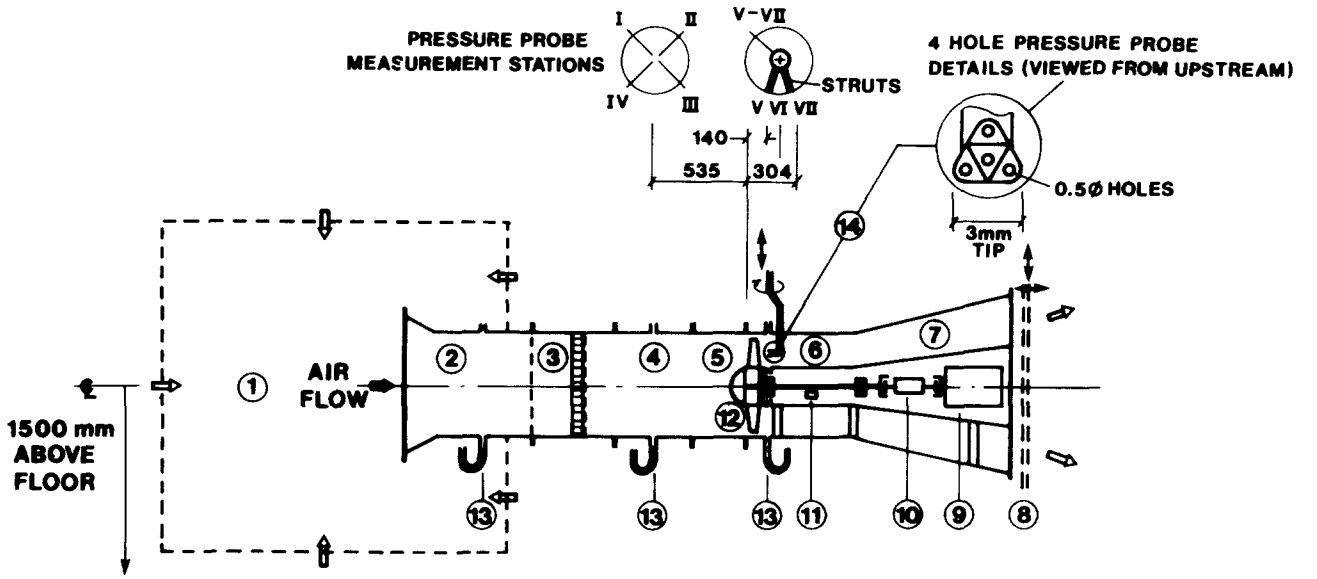

1,	Screen box	2 m sides, woven 0.1 mm thread × 2.5 pores/lin. mm
2,	BS 848 conical inlet	1.25D long
3,	Flow conditioning module	0.75D long, includes: 16 S.W.G. No. 3 wire woven screen, 65% open area; antiswirl honeycomb element, hexagonal cells, 4.5 mm sides × 75 mm deep; turbulence reduction screen, woven 0.1 mm thread × 1 pore/lin. mm
4,	Fan inlet duct	0.75D long
5,	Flow visualization module	0.5D long (optional)
6,	Fan tube (D = 610 mm)	1.0D long; diameter D, centerbody diameter 0.38D
7,	Annular diffuser	1.6D long: outer included angle 27°; inner included angle 16°
8,	Adjustable screens	No. 1 fancy pattern perforated sheet, 36% open area
9,	Electric motor	4 kW, four-pole motor with static frequency converter speed control
10,	Torque transducer	0–5 Nm capacity
11,	Shaft speed transducer	Optoelectronic sensor
12,	Fan test rotor	Nose fairing 135 mm radius × 75 mm deep
13,	Static pressure tappings	Four equispaced wall tappings
14,	Pressure probe	Four-hole Cobra pressure probe

Figure 3. "Arbitrary vortex flow" fan test rig aerodynamic outline.

direct-exhaust fan/rotor configuration tests, exceeds the requirements for testing fans to the Australian Standard [5] using the Inlet Chamber Assembly method. An aerodynamic outline of this test facility is shown in Fig. 4.

A booster fan (*1*) draws in laboratory air, which passes through a fan diffuser section (*2*) and then discharges into a plenum chamber (*3*). The air then passes through the chamber assembly, where it encounters a series of flow settling screens (*4*), a set of 10 ASHRAE Standard flow measuring nozzles [13] mounted in a partition wall (*5*), a second series of flow settling screens (*6*), a honeycomb flow straightener (*7*), and a final series of turbulence reduction and flow settling screens (*8*) prior to entering the test fan inlet plenum chamber (*9*).

The test rotor (*10*) is mounted, for example, in a bellmouth inlet assembly (*11*), which is set into the end wall of the fan inlet chamber. The rotor drive system (*12–14*) is similar in principle to that used in the arbitrary vortex flow fan test rig.

Static pressure measuring stations, consisting of sets of four equispaced plenum wall tappings, are located immediately upstream and downstream of the nozzle set (*15*, *16*) and on the fan inlet plenum chamber (*17*).

Instrumentation

The instrumentation is illustrated, in part, in the aerodynamic outlines shown in Figs. 3 and 4. A compact four-hole Cobra pressure probe assembly (Fig. 3, *14*) is used on the arbitrary vortex flow rig to provide flow direction (yaw and pitch components), flow velocity, and total pressure data [14] as the pressure probe is traversed across the fan inlet duct or across the fan annulus in the vicinity of the trailing edge of the low solidity blading. The pressure probe is used in a non-nulling or "fixed-angle" mode after being calibrated at fixed yaw and pitch angle combinations in a 244 mm square working section of a blowdown, open-discharge air tunnel at a nominal flow velocity of 9.5 m/s. Checks at an approximate flow velocity of 13.5 m/s indicated that the Cobra pressure probe calibration was essentially independent of Reynolds number in this veloc-

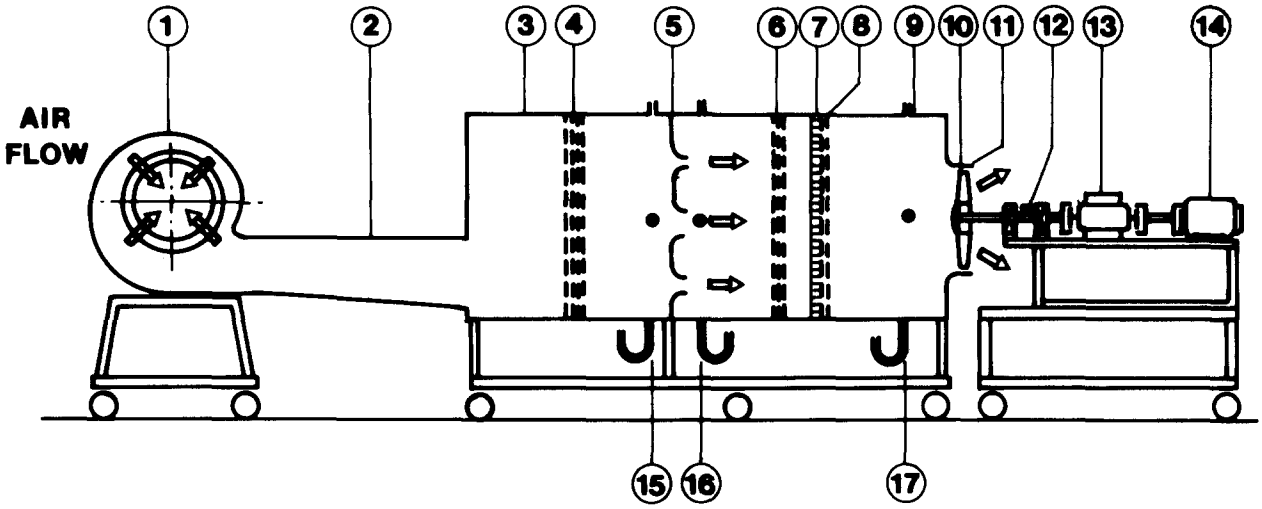

1, Auxiliary or booster fan;
2, Auxiliary fan diffuser;
3, Plenum chamber;
4, Flow settling screens: one No. 1 fancy pattern perforated sheet, 36% open area; three fabric screens, woven 0.1 mm thread × 1 pore/lin. mm;
5, Flow measuring nozzles: 10 nozzles, 25–103 mm diameter ASHRAE 51–75;
6, Flow settling screens: one perforated sheet, 46% open area; one fabric screen, woven 0.1 mm thread × 1 pore/lin. mm; one perforated sheet, 51% open area;
7, Antiswirl element; hexagonal cells, 4.5 mm sides × 75 mm deep;
8, Turbulence reduction and flow settling screens: fabric screens, woven 0.1 mm thread × 1 pore/lin. mm;
9, Test fan inlet chamber;
10, Fan test rotor;
11, Bellmouth entry;
12, Shaft speed transducer, optoelectronic sensor;
13, Torque transducer, 0–5 Nm capacity;
14, Electric motor; 1.1 kW, four-pole motor with static frequency converter speed control;
15, Static pressure tappings upstream of nozzles;
16, Static pressure tappings downstream of nozzles;
17, Static pressure tappings test fan inlet chamber.

Figure 4. Fan inlet chamber assembly test facility aerodynamic outline.

ity range. The mean annulus velocity at the test rotor design condition was approximately 7.5 m/s.

The instrumentation systems for both test rigs are essentially the same except that the Cobra pressure probe is used only with the arbitrary vortex flow rig. High-resolution, low-pressure-range transducers are used in conjunction with the conical inlet, the Cobra pressure probe, and the duct and plenum chamber wall static pressure tappings. These pressure transducers were regularly calibrated against a precision micromanometer, and the torque transducers were calibrated at representative rotor test speeds using a rope brake type device. The shaft rotational speed modules incorporate an optoelectronic sensor unit and rely on the data acquisition system clock for accurate time interval determinations.

A Digital Equipment Corporation (DEC) PDP11/44 computer system fitted with an LPA11 digitizing system and an Interactive Laboratory Systems (ILS) software package were used for high-speed data acquisition and online data processing during the experimental program.

Arbitrary Vortex Flow Rig Test Procedures

The purpose of the arbitrary vortex flow rig was to establish the spanwise blade element performance (outside of the wall boundary layer regions) of the three experimental rotors for both on-design and off-design fan operating duties, that is, differing combinations of fan volume airflow rate and fan total pressure rise at constant-speed operation. Each rotor was tested at its design blade setting or pitch angle, which corresponds to blade setting angles at the blade midspan of ϕ_p = 23.3°, 23.5°, and 22.5° for the Mark 1, 2, and 3 rotors, respectively. It should be noted that "free-discharge" fan operating conditions cannot be obtained in the arbitrary vortex flow fan test rig because of the significant pressure loss associated with the flow conditioning module (*3*) upstream of the rotor (Fig. 3).

The blade tip clearances for the three rotors were in the range 1.0–1.7 mm (corresponding to rotor tip clearance ratios based on blade span of t_c = 0.5–0.9%), and the

blade root clearances were a minimum, consistent with a requirement that the blade pitch be adjustable on a cylindrical hub over a range of approximately $\pm 8°$ from the design blade setting angle.

The fan rotor test speed was 1000 ± 2 rpm, which corresponds to blade Reynolds numbers [5] based on the blade tip chord of approximately 2.2×10^5 for the Mark 1 rotor and 2.5×10^5 for the Mark 2 and 3 rotors.

The Cobra pressure probe was progressively traversed radially through typically 20 point locations lying on a single radial line within the fan annulus, for example, measurement station V (Fig. 3). At each measurement point the transducer output signals were logged concurrently over a 16 s period at a rate of 500 samples/s for each transducer. This logging duration was chosen after investigating the reproducibility of the results in the presence of the typical flow structures moving downstream from the rotor. These sampled data were reduced online to provide mean and standard deviation values for the pressure and torque transducer signals. Transducer zero offsets were measured at regular intervals and applied to sampled mean data values to minimize the effect of transducer and/or data acquisition circuitry zero drifts. The above data acquisition technique provides time-averaged "mean" results, as the sampling was not initiated to coincide with the blade passing frequency.

Fan Inlet Chamber Assembly Test Procedures

The Mark 3 rotor (without nose fairing) was installed in a direct-exhaust fan/rotor configuration and tested using the fan inlet chamber assembly (Fig. 4) to quantify the fan/rotor mean performance characteristics over a range of blade setting angles. The rotor blade trailing edges at the blade tip section were situated just within the throat section of the bellmouth for each of the blade setting angles tested.

The Mark 3 fan/rotor direct-exhaust configuration performance characteristics have been established in terms of fan inlet volume flow rate and fan inlet total pressure (previously known as fan static pressure [1, 5]) for blade setting angles (at the nominal midspan location) of $\phi_p =$ 18°, 24°, 30°, 36°, and 42°. For the duration of these tests the rotor was configured with a nominal blade tip clearance of 2.5 mm ($t_c = 1.3\%$) in a 612 mm diameter end-wall-mounted bellmouth comprising a 150 mm inlet radius section and a 100 mm long parallel throat section. The blade root clearance was increased to enable the blades to accommodate the highest setting angle of 42°.

The effect of rotor tip clearance on the direct-exhaust performance of the Mark 3 fan/rotor has also been established at one blade setting angle, $\phi_p = 24°$, with the rotor installed in a 617 mm diameter end-wall-mounted bellmouth comprising a 43 mm inlet radius section and a 64 mm long parallel throat section. The blade tip clearance was varied in the range 1–5 mm ($t_c = 0.6$–2.5%) by adhering solid, fully profiled extensions to the blade tips to achieve the required tip clearance.

Each fan inlet chamber assembly test was conducted at constant shaft rotational speed conditions. However, because the maximum airflow rate capability of the facility is approximately 1.1 m^3/s, the test rotor operating speed must be limited to enable testing to include free-discharge conditions. A speed of 580 rpm was used for the 18° blade setting angle, being progressively reduced to 310 rpm for the 42° blade setting angle, which corresponds to blade Reynolds numbers (based on the blade tip chord) of approximately 1.5×10^5 and 0.8×10^5, respectively.

Test Rig Commissioning

The arbitrary vortex flow fan test rig (Fig. 3) underwent extensive commissioning, and it was found necessary to incorporate the screen box (*1*) and the upstream screen (*3*) to obtain uniform flow velocity profiles at Cobra pressure probe measurement stations I–IV in the fan inlet duct upstream of the rotor nose fairing. Subsequently the axial velocity profile data derived from the Cobra pressure probe measurements along the four radii in the fan inlet duct were integrated using an area-weighted basis [9], and the implied airflow rate for the cross section was found to agree, within 3%, with the fan inlet volume flow rate measured using the BS conical inlet method [11]. The corresponding flow pitch and yaw angle data (outside of the wall boundary layer) were within $\pm 1.5°$ with respect to the duct centerline axis. The static pressure distributions derived from the Cobra pressure probe measurements were found to be in acceptable agreement with the corresponding measured wall static pressure.

The size of the Cobra pressure probe head becomes a limiting factor in highly sheared flows, and the following discussion is, in general, restricted to the spanwise region between the centerbody and outer wall boundary layers. In the case of a low boss ratio, low solidity rotor operating at or near the design duty condition, the time-averaged mean flow properties across such a region downstream of a rotor can be expected to be essentially uniform, with typically less than 10% of the sampled data collected in the presence of a blade wake passing.

Cobra pressure probe surveys were conducted at measurement stations V–VII in the fan annulus (Fig. 3) downstream of the Mark 1 test rotor for a range of rotor operating conditions. The static pressure distributions derived from the Cobra pressure probe measurements were found to be in acceptable agreement with the corresponding measured duct wall and centerbody static pressures. Station V was located the equivalent of approximately half the blade chord (blade midspan basis) distance downstream from the rotor blade trailing edge, which corresponds to the closest position recommended in Ref. 1 for reliable total pressure rise measurements. Stations VI and VII were situated further downstream, at approximately one and two midspan blade chord distances from the rotor blade trailing edge, respectively.

For the rotor design flow case, significant differences occurred between some of the spanwise flow data distributions at stations V, VI, and VII. The flow yaw angle distribution reduced progressively between stations V and VII by approximately 5° in 30°, whereas the flow pitch angle distribution reduced by approximately 2° in 10° between stations V and VI, and remained nearly constant between stations VI and VII. The total pressure rise coefficient distribution remained nearly constant for all three measuring stations, which is consistent with data presented by Wallis [1]. The derived downstream axial velocity ratio distribution did not vary significantly be-

tween the three measurement stations, and the implied airflow rates calculated from these distributions (including wall boundary layer regions) were found to agree with the measured fan inlet volume flow rate to within 4%. The derived tangential (swirl) velocity ratio distribution reduced progressively by approximately 10% between successive measurement stations.

The integrated elemental rotor torque corresponding to the tangential velocity ratio distribution at station V (including wall boundary layer regions) was found to be of the order of 10% below the measured rotor shaft torque. Thus, it is concluded that the magnitude of the tangential (swirl) velocity ratio at the rotor exit plane is significantly underestimated when the flow yaw angle data measured at station V are used to determine the tangential velocity ratio distribution. However, station V was subsequently chosen as being the most practical and representative for local flow measurements downstream of the rotor for the design flow case, and these measurements are considered to represent useful approximations, with the above caution, to the mean flow properties at the trailing edge plane for this low solidity rotor.

Similar surveys at stations V–VII for the rotor operating near the onset of stall and into the stall region indicated that the distributions of flow velocity, flow direction, and total pressure varied significantly between the stations, with the axial velocity ratio distributions becoming progressively skewed toward the outboard region of the blade span as the measurement plane was moved further downstream of the rotor. At each of the higher fan pressure loadings, the tangential velocity ratio distributions reduced progressively between successive measurement stations, but at a lesser rate (to below 5%) than that observed for the design flow case, while the total pressure distributions also reduced progressively between measuring stations. Although the trends disclosed in the measured data corresponding to off-design flow conditions can be considered indicative, discrepancies between the measured distributions at station V and the flow properties at the trailing edge of the rotor (rotor exit plane) may increase under these conditions.

The fan inlet chamber assembly test facility generally exceeds the minimum performance requirements as prescribed in the relevant Australian Standard [5]. The integrity of the airflow measurement capability of this rig fitted with the multiple-nozzle configuration has been confirmed by comprehensive comparison calibrations against a 254 mm diameter British Standard orifice plate installed in a 380 mm diameter straight duct run in accordance with BS 1042 [15].

UNCERTAINTY ANALYSIS

The estimated measurement uncertainty (to 95% confidence limits) pertaining to the instruments used in the test program is given in Table 1 and is based on the method proposed by Kline and McClintock [16].

The estimated overall uncertainty (to 95% confidence limits) pertaining to the data presented from the experimental program is given in Table 2 and is based on the method proposed in Ref. 16. In the case of derived spanwise distributions of downstream velocity ratio and rotor pressure rise coefficient, the respective uncertainty estimates correspond to the rotor midspan region, it being assumed that the Cobra pressure probe is operating in the presence of essentially uniform flow in the region between the centerbody and duct wall boundary layers downstream of the rotor. The uncertainty estimates for the derived rotor performance characteristics (ψ_R and η_R) are based on the rotor midspan region estimates, which are assumed to be representative of the flow over the complete fan annulus.

Table 1. Measurement Uncertainty Estimates

Transducer / Instrument	*Uncertainty Estimate*
Arbitrary Vortex Flow Fan Test Rig	
Airflow rate (BS conical inlet)	$< \pm 2.5\%$[a]
Pressure transducers (above 1/4 full-scale)	$< \pm 2.0\%$[a]
Shaft torque	$< \pm 1.0\%$[a]
Shaft rotational speed	$< \pm 0.05\%$[a]
Fan Inlet Chamber Assembly Test Facility	
Airflow rate (ASHRAE nozzles)	$< \pm 1.3\%$[a]
Pressure transducer	
Near fan peak pressure duty	$< \pm 1.2\%$[a]
Near fan free-discharge pressure duty	$< \pm 3.5\%$[a]
Shaft torque	$< \pm 1.1\%$[a]
Shaft rotational speed	$< \pm 0.15\%$[a]
Cobra Pressure Probe[b]	
Flow pitch angle	$< \pm 2°$
Flow yaw angle	$< \pm 3°$
Flow velocity	$< \pm 3\%$[a]
Flow total pressure	$< \pm 3\%$[a]
Miscellaneous	
Barometer	$< \pm 0.2$ kPa
Air temperature	$< \pm 1°$C
Blade setting angle jig	$< \pm 0.2°$

[a] Of measured value.
[b] In 9.5 m/s uniform velocity profile airstream.

EXPERIMENTAL RESULTS

For axial rotor design purposes, the fan volume flow rate can be converted to the rotor nondimensional tip flow coefficient Λ, and local velocity components can be converted to nondimensional velocity ratios in terms of $\bar{V}_a$ [1]. Similarly, local pressure data can be converted to nondimensional pressure coefficients k in terms of the simple axial velocity pressure $(1/2)\rho\bar{V}_a^2$, and the blade element position can be specified in terms of a nondimensional radius ratio x [1].

For commercial fan applications, it is more convenient to define nondimensional coefficients in terms of the fan diameter, shaft rotational speed, and air density. The fan inlet volume flow rate and the fan total pressure (rise) or fan inlet total pressure (rise) can be expressed in nondimensional terms as a fan volume flow rate coefficient Φ, and fan pressure coefficients ψ_T and ψ_E, respectively [5].

Mark 1, 2, and 3 Rotor Spanwise Performance Trends

The rotors were tested in the arbitrary vortex flow test rig (Fig. 3) over the range $\Lambda = 0.15$–0.255, and selected re-

Table 2. Experimental Data Uncertainty Estimates

Experimental Data	*Uncertainty Estimate*
Arbitrary Vortex Flow Fan Test Rig	
Radius ratio	$< \pm 0.001$
Local Axial velocity ratio ($\Lambda = 0.23$)	$< \pm 5\%$[a]
Local tangential velocity ratio ($\Lambda = 0.23$)	$< \pm 9\%$[a]
Local radial velocity ratio ($\Lambda = 0.23$)	$< \pm 40\%$[a]
Local rotor total pressure rise coefficient k_r ($\Lambda = 0.23$[b])	$< \pm 5.5\%$[a]
Local rotor static pressure rise coefficient ($\Lambda = 0.23$)	$< \pm 7.5\%$[a]
Fan volume flow rate coefficient Φ	$< \pm 2.5\%$[a]
Rotor total pressure rise coefficient ψ_R ($\Lambda = 0.23$, iv[b])	$< \pm 6\%$[a]
Rotor efficiency, total η_R ($\Lambda = 0.23$, iv[b])	$< \pm 6.5\%$[a]
Fan Inlet Chamber Assembly Test Facility	
Fan volume flow rate coefficient Φ	$< \pm 1.3\%$[a]
FITP coefficient ψ_E (near peak fan pressure)	$< \pm 1.2\%$[a]
FITP coefficient ψ_E (near free-discharge pressure)	$< \pm 3.5\%$[a]
Fan efficiency, exhaust η_E (near peak fan pressure)	$< \pm 1.1\%$[a]

[a] Of calculated value.
[b] Refer to Figs. 7 and 8.

sults are presented in Figs. 5–8. The wall boundary condition values corresponding to $x = 0.38$ and 1.00 are included in the figures, and in the case of the total and static pressure rise coefficient data these have been derived from measured duct wall and centerbody static tapping pressures. The implied airflow rates calculated from the downstream axial velocity ratio distributions (including wall boundary layer regions) (Figs. 5*a*, 6*a*, and 7*a*), were always found to agree with the measured fan inlet volume flow rate to within 4.5%. The rotor total and static pressure rise distributions (Figs. 5*d*, 5*e*, 6*d*, 6*e*, 7*d*, and 7*e*) represent the respective pressure changes across the rotor blading with respect to a reference plane situated in the fan annulus upstream of the rotor. These data were derived from measurements at the static wall tappings in the fan inlet duct and at the fan annulus measurement station V plane, using the assumption that the total pressure losses as the flow enters the fan annulus are negligible. A flow coefficient $\Lambda = 0.23$ corresponds approximately to the design flow condition for each rotor. The Mark 1 and 2 rotors are operating in the stall region at $\Lambda < 0.18$.

In the case of the Mark 1 rotor, the flow in the hub vicinity remains attached at the lower pressure duties (higher flow coefficients), but reverse flow is evident downstream of the hub at the higher fan pressure rise loadings (Fig. 5*a*). The boundary layers on the outer duct wall and the centerbody become appreciably thicker at higher pressure rise operating conditions, and to satisfy continuity the downstream axial velocity ratios are seen to be augmented between the wall boundary layers. The spanwise local tangential (swirl) velocity ratio approximates to a linear distribution over the major portion of the blade span (ie, outside the wall boundary layer regions) even up the higher pressure load duties (Fig. 5*b*). At the design condition, the radial flow component pitch angle is found to be approximately 4°. However, major changes occur once the inboard downstream axial velocity components become negative, with the flow pitch angle attaining a peak of approximately 15° for the $\Lambda = 0.15$ flow condition, as reflected in the radial velocity data presented in Fig. 5*c*.

The spanwise position at which the local total pressure rise equals the mean value is approximately $x = 0.72$ for the Λ range 0.255–0.21 (Fig. 5*d*). The calculated peak rotor total efficiency (based on the mean total pressure rise across the blading, including the swirl component) is approximately 86% and corresponds to Λ in the range 0.23–0.24. When the swirl component is excluded, the calculated peak rotor efficiency falls to approximately 77% and again occurs at Λ values between 0.23 and 0.24.

Similar radial flow characteristics were recorded for the Mark 2 design rotor case (Fig. 6*c*), but as the stall is approached the increase in radial flow is more restrained across the blade span. The total pressure duty capabilities of the Mark 2 rotor are superior to those of the Mark 1 unit across the whole of the operating range investigated, especially in the stall onset region (Figs. 5*d* and 6*d*). The Mark 2 peak rotor total pressure efficiencies (85% with the swirl component included and 75% with the swirl component excluded) are similar to that achieved in the Mark 1 unit, but the falloff in efficiency and shaft power are far less pronounced over the operating range tested.

The Mark 3 rotor is superior in performance to both the Mark 1 and 2 rotors as the stall is approached, with lower peak swirl values at the blade tip (Fig. 7*b*). The falloff in the inboard axial velocity components (as the stall is approached) in the Mark 3 rotor (Fig. 7*a*) results in increased radial velocity components as shown in Fig. 7*c*. A notable feature of the Mark 3 blading is the absence of the large blade tip vortex as implied by the trough in the velocity distributions (Figs. 5*a*, 6*a*, and 7*a*). The ability of airfoil blades such as the F-series to outperform cambered plate blades, particularly in respect to the maximum lift attainable, is well known. The result is a significant increase in the maximum total pressure rise obtained at the stall condition, with a slightly steeper characteristic curve than for the first two rotors. An apparent increase in the calculated peak rotor total pressure efficiencies to 89 and

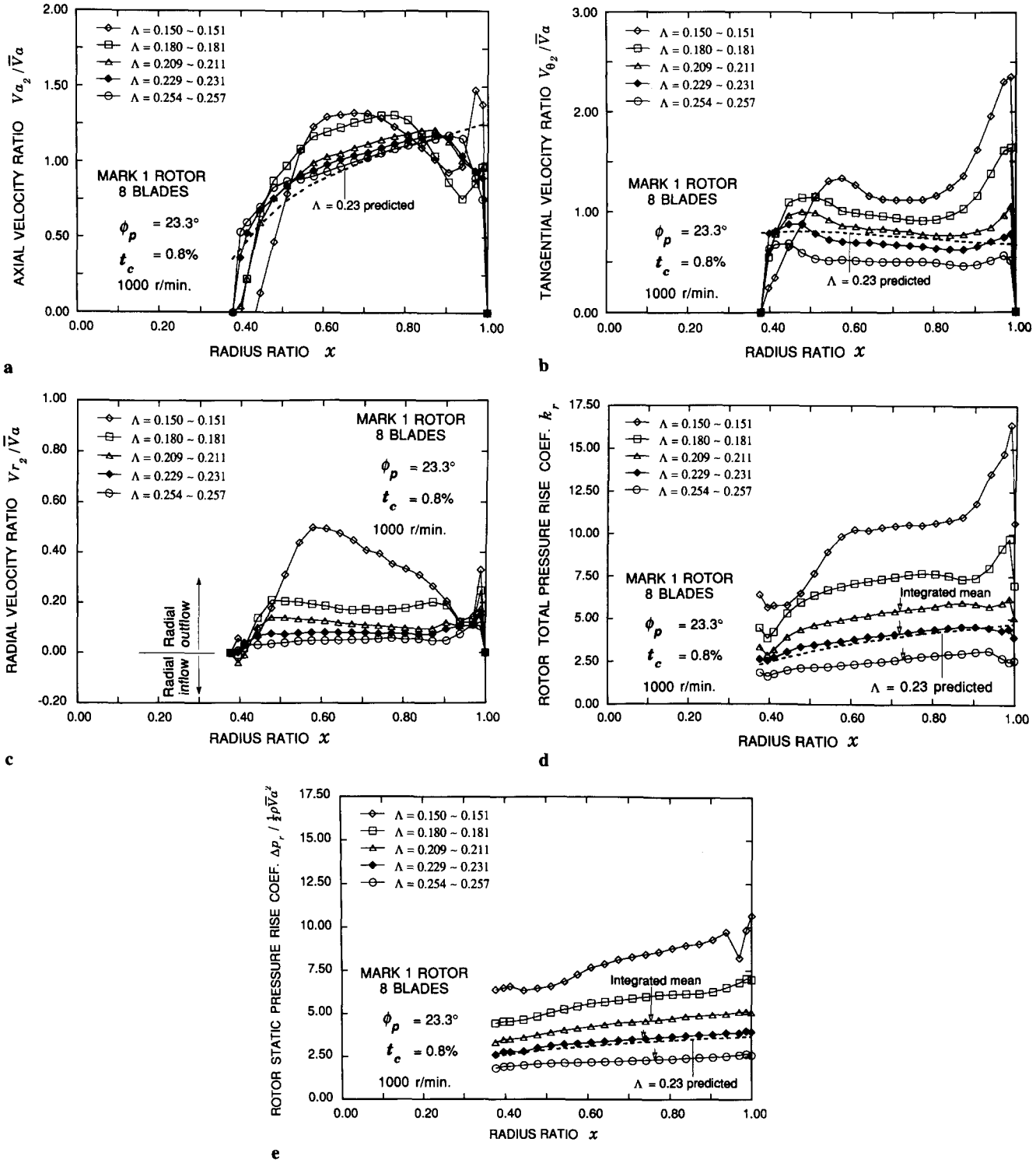

Figure 5. Spanwise distributions downstream of the Mark 1 rotor. (*a*) Axial velocity ratio; (*b*) tangential velocity ratio; (*c*) radial velocity ratio; (*d*) rotor total pressure rise coefficient; (*e*) rotor static pressure rise coefficient.

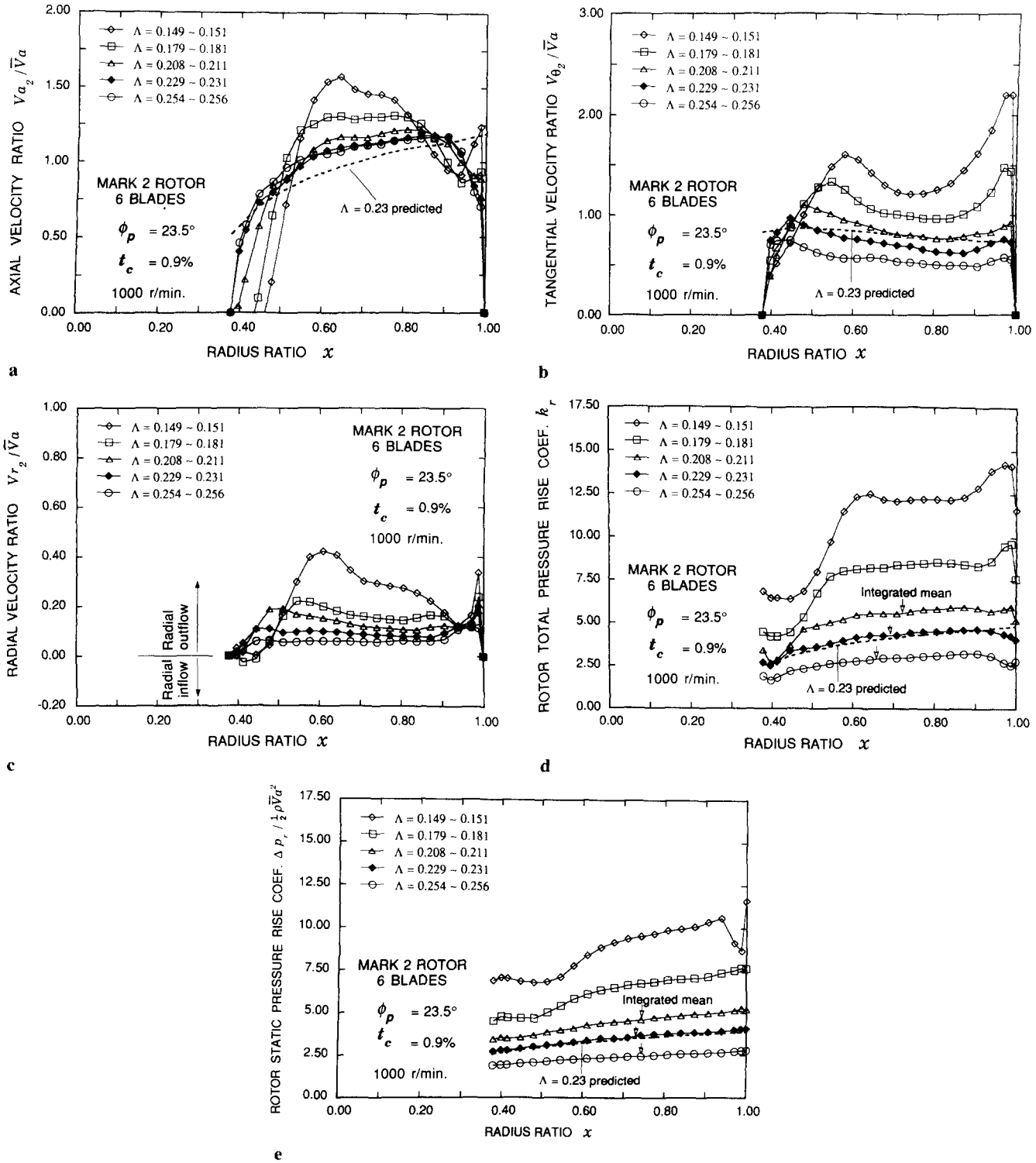

Figure 6. Spanwise distributions downstream of the Mark 2 rotor. (*a*) Axial velocity ratio; (*b*) tangential velocity ratio; (*c*) radial velocity ratio; (*d*) rotor total pressure rise coefficient; (*e*) rotor static pressure rise coefficient.

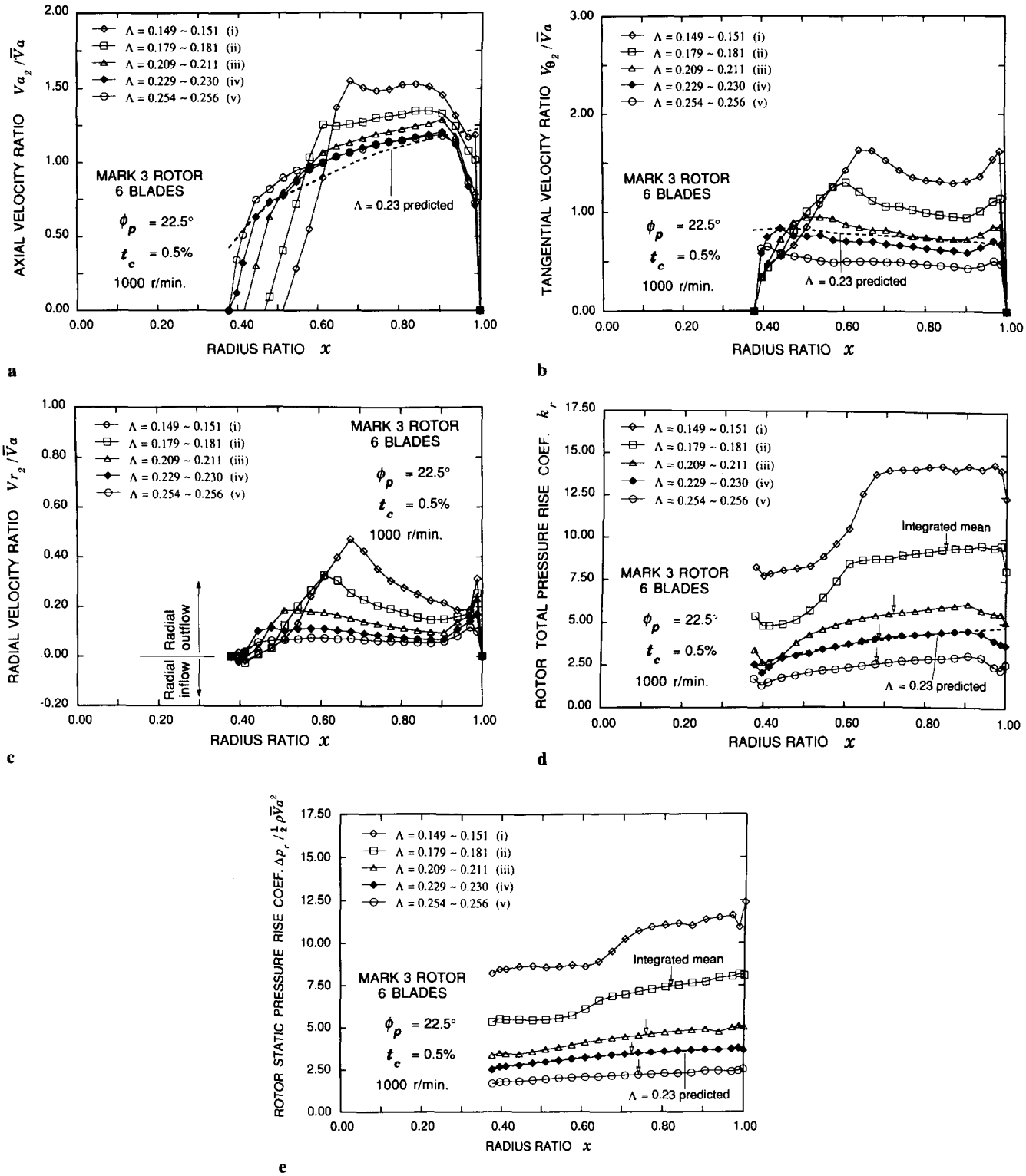

Figure 7. Spanwise distributions downstream of the Mark 3 rotor. (*a*) Axial velocity ratio; (*b*) tangential velocity ratio; (*c*) radial velocity ratio; (*d*) rotor total pressure rise coefficient; (*e*) rotor static pressure rise coefficient [operating points (i)–(v); refer also to Fig. 8].

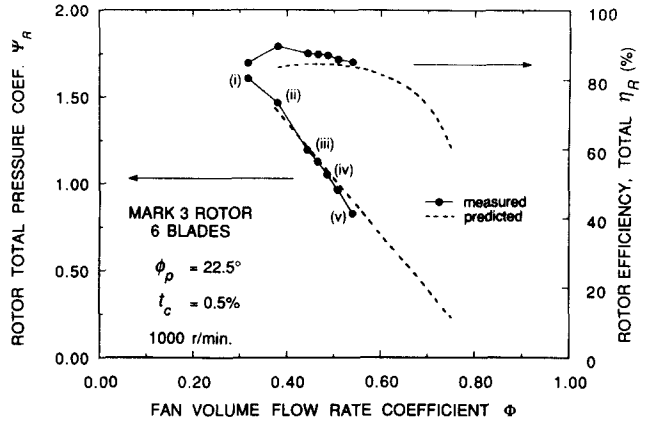

Figure 8. Comparison of the measured and the predicted blading performance characteristics for the Mark 3 rotor.

78%, respectively, with and without the swirl component included, were obtained with the Mark 3 rotor.

Mark 3 Fan / Rotor Performance Characteristics

The Mark 3 rotor was also tested in a direct-exhaust configuration (Fig. 4); the measured fan performance characteristics are shown in Figs. 9*a* and 9*b* for a range of midspan blade setting angles between ϕ_p = 18° and 42°. The fan inlet total pressure capability toward the stall region is maintained for the higher blade setting angles (Fig. 9*a*). Peak exhaust efficiencies (based on the fan inlet total pressure) of approximately 57% were obtained for blade setting angles in the region of the design pitch angle (Fig. 9*b*).

The effect of varying blade tip clearance was investigated using the Mark 3 rotor. An optimum blade tip clearance for such a rotor is thought to be of the order of t_c = 0.5–1.0% [1]. Figure 10 shows the measured performance of the Mark 3 rotor, in essentially the same direct-exhaust configuration (Fig. 4), with the blading set at ϕ_p = 24° and for a range of rotor tip clearance ratios t_c between approximately 0.5 and 2.5%. The zero pressure rise performance is shown to be essentially insensitive to rotor tip clearance variations over the range tested. However, increases in rotor tip clearance ratio cause significant reductions in the fan inlet total pressure capability as the fan pressure increases. Figure 11 presents these data in terms of a pressure loss ratio (the ratio of the fan inlet total pressure loss due to rotor tip clearance effects $t_c >$ 0.5% to the fan inlet total pressure capability at t_c = 0.5%) as a function of the rotor tip clearance ratio t_c and the operating system resistance (typified by the system resistance curves in Fig. 10, which follow the square law). A reduction in fan inlet total pressure capability of the order of 20% nearing the stall region was found to result from increasing the rotor tip clearance from approximately 0.5% to 2.5%.

NUMERICAL ANALYSIS RESULTS AND COMPARISONS

Mark 1, 2, and 3 Rotor Performance Predictions

The most important rotor design parameters are embodied in the spanwise distributions of downstream tangential

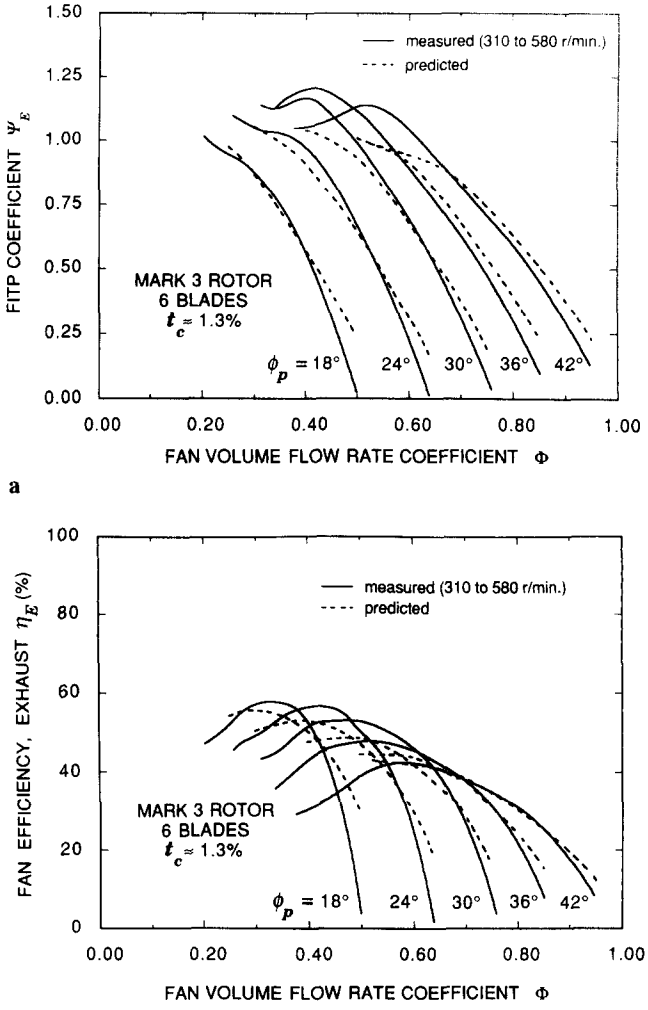

Figure 9. Comparison of the measured and predicted fan performance characteristics for the Mark 3 rotor mounted in a direct-exhausting fan configuration. (*a*) Fan inlet total pressure; (*b*) exhaust efficiency.

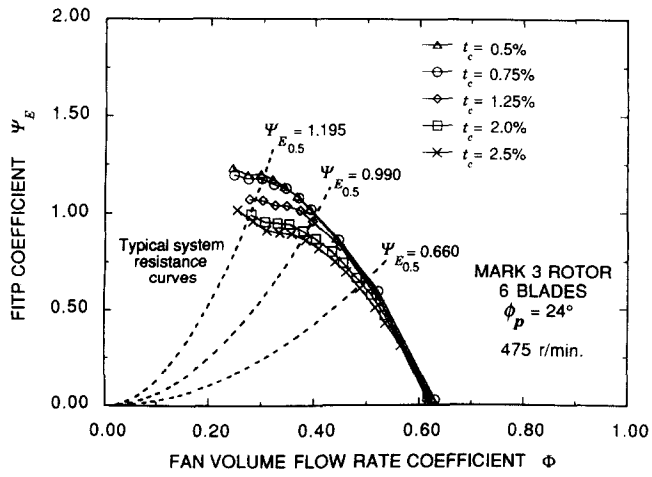

Figure 10. Effect of varying blade tip clearance ratio on the fan inlet total pressure performance characteristic for a Mark 3 rotor mounted in a direct-exhausting fan configuration.

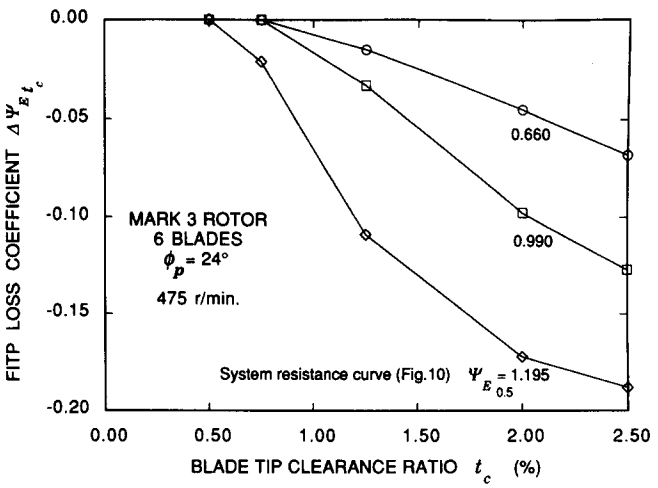

Figure 11. Fan inlet total pressure loss coefficient versus blade tip clearance ratio for a Mark 3 rotor mounted in a direct-exhaust fan configuration.

(swirl) velocity, downstream axial velocity, and total pressure rise across the rotor. The predicted distributions corresponding to the rotor (design) tip flow coefficient ($\Lambda = 0.23$) are superimposed on the measured rotor performance data (Figs. 5–7). These predictions are the result of the iterative analytical procedures previously described, with 11 equally spaced blade element positions across the blade span being used for the analysis calculations. The best-fit swirl coefficient distribution was considered achieved when the two calculated distributions of lift coefficient agreed within the equivalent of a weighted least-squares error of less than 0.03 and the value for the rotor total efficiency had converged to within 0.0025. When comparing the predicted and measured distributions it must be realized that the design method does not model the complex wall boundary layer regions, and thus the following comments are restricted to that part of the blade span between these wall boundary layer regions.

The predicted swirl distributions (Figs. 5*b*, 6*b*, and 7*b*) are seen to exceed those measured at pressure probe station V. During the commissioning it was found that the integrated torque obtained from measured swirl distribution at station V was approximately 10% less than that measured by the shaft torque transducer. The measured swirl distributions must therefore be adjusted accordingly to obtain the corresponding distributions at the exit plane of the rotor. If this correction were applied, then the predicted and measured swirl distributions would agree to within a few percent over most of the blade span.

The downstream axial velocity ratio distribution predictions (Figs. 5*a*, 6*a*, and 7*a*) indicate reasonable agreement on the outer blade region, but the axial flow component over the inboard and midspan regions of the blades is found to be underestimated (by up to 12% in the Mark 2 case). Simplifying the design method by neglecting the effect of the wall boundary layers is at least partially responsible for this discrepancy, as any attempt to model the wall boundary layers would certainly result in predicted flow increases in the central blade span regions to meet mass conservation requirements. Nevertheless, the rotor total and static pressure rise predictions are seen to closely match the respective measured distributions (Figs. 5*d*, 5*e*, 6*d*, 6*e*, 7*d*, and 7*e*) and are considered to be acceptable for engineering design purposes.

The analytical method for this particular case is seen to adequately predict representative rotor total pressure rise (with the swirl component included) and rotor total efficiency characteristics for the Mark 3 rotor corresponding to a wide range of pressure duties up to the approach of stall (Fig. 8). At volume flow rates below approximately $\Phi = 0.4$, the analytical method predicts that flow will cease over the inboard blade regions beginning at the blade root.

Mark 3 Fan / Rotor Performance Predictions for the Direct-Exhaust Case

Such a design and analysis method becomes an even more valuable tool when it is able to provide meaningful performance estimates for arbitrary vortex flow rotor-only installations, including rotors with variable pitch blading and direct-exhaust applications with higher than zero loss rotor tip clearances.

The ability of the method to address direct-exhaust rotor-only configurations with a wide range of blade setting angles has been investigated, and Figs. 9*a* and 9*b* show a comparison of the measured and predicted fan performance characteristics for the Mark 3 rotor with the blade setting angles in the range $\phi_p = 18$–42%. The fan inlet total pressure and exhaust efficiency predictions (Figs. 9*a* and 9*b*) are in acceptable agreement over the range of blade setting angles investigated and in general vary from being somewhat optimistic near free discharge to being conservative near the onset of stall. The predictions at pressure loadings exceeding $\psi_E \approx 0.85$ correspond to where the flow over the inboard blade regions is predicted to cease. There is also uncertainty with respect to the lift and drag data currently used for the F-series airfoils, as they are based on wind tunnel test data for C4 and NACA series airfoils [6]. Similarly, wind tunnel test data for these airfoils operating in low Reynolds number regimes are not yet available.

As noted earlier, a flow rate limitation associated with the inlet chamber assembly test facility resulted in the Mark 3 fan/rotor direct-exhaust configuration being tested at relatively low rotor speeds in the range 310–580 rpm, which corresponds to blade Reynolds numbers of between 8×10^4 and 1.6×10^5 (based on the blade tip chord). These are below the critical Reynolds number regime (2.5×10^5) reported for airfoil blades with low inlet turbulence [1] and outside the range of the lift/drag data for smooth 10% thick cambered airfoils available in [1]. The maximum lift capability and the minimum profile drag regions are both known to change significantly for many airfoils in these low Reynolds number regimes [7, 8]. Similar data are not available for the C4 or F-series airfoils. However, the profile drag estimates used for the above predictions (Fig. 9) have been extrapolated from trends presented in Fig. 6.10 of Ref. 1.

Performance Prediction Comparisons: The Midspan Approximation Versus the Integrated Spanwise Method

Figure 12 shows a comparison of measured and predicted fan performance characteristics for the Mark 3 rotor

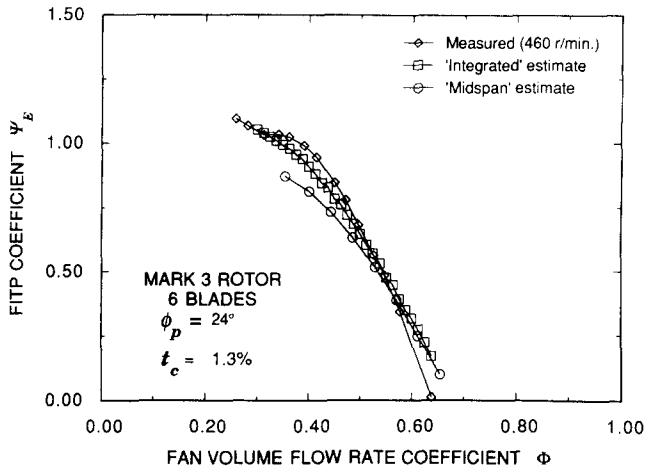

Figure 12. Comparison of measured and predicted fan inlet total pressure performance characteristics for a Mark 3 rotor mounted in a direct-exhaust fan configuration.

mounted in the previously described direct-exhaust configuration. The "midspan" estimate is based on Wallis's method [1], where the calculations are simplified by assuming that

- The local rotor total pressure rise at the blade midspan provides an adequate and reliable estimate of the mean total pressure rise across the rotor.
- The spanwise swirl is appoximated by a linear distribution.
- The velocity pressure components immediately downstream of the rotor comprising the simple axial velocity pressure within the fan annulus, $(1/2)\rho\bar{V}_a^2$, and the midspan downstream tangential velocity pressure are irrecoverable in the direct-exhaust configuration in question.

The "integrated" estimate is obtained using the analysis algorithm previously described. The predicted rotor total pressure rise and downstream axial and tangential velocity pressure distributions are integrated using the mass-weighted technique [9], where the two velocity pressure components mentioned above are again assumed to be irrecoverable in the direct-exhaust configuration in question.

The predicted curves were developed by first addressing the free-discharge region and then progressively working toward lower flow rate conditions. The calculations were terminated when the iterative procedure (described earlier) failed to converge. This occurs when the radial equilibrium equation solution predicts that through-flow has ceased over a significant portion of the inboard region of the blade. The two performance predictions include an allowance for the effect of rotor tip clearance as described in the Appendix.

Figure 12 indicates that both techniques overestimate the free-discharge and low pressure duty capabilities of the fan/rotor combination. The midspan method predictions become conservative at the higher pressure duties, whereas the integrated method is able to better predict the fan/rotor performance over the region between the rotor design flow rate ($\Phi = 0.5$) and the onset of stall, which is an important operational region in many fan applications.

DISCUSSION

As a result of the experimental program with the Mark 1, 2, and 3 rotors, important matters relevant to the arbitrary vortex flow design procedure proposed in Ref. 1 have either been confirmed or are subject to modification. In particular, the detailed test program has resulted in the establishment of limits for several design parameters. The absence of such empirical guidelines relegated the subject of arbitrary vortex flow design to an appendix in Ref. 1.

The major points arising out of the experimental program are summarized below.

1. The radial velocity component can be ignored for the purpose of formulating the radial equilibrium equation because the measured values of this velocity component corresponding to the rotor blade design case are typically less than 10% of the downstream axial velocity component value. The resulting radial velocity pressure component is therefore less than 1% of the axial velocity pressure component and hence is of the same order as other inaccuracies resulting from the design assumptions.
2. The design/analysis technique adequately predicts the measured distributions of swirl (corrected to the rotor exit plane) for the design case, with the exception of the blade extremities where secondary flows are present. More important, it is also able to provide adequate estimates of the rotor total pressure rise over a range of operating conditions. Thus, for the purpose of arbitrary vortex flow rotor design and analysis it is considered satisfactory to assume that the redistribution of axial and tangential velocity components is essentially complete immediately downstream of the blading and that the arithmetic mean of the upstream and downstream axial velocity components, at any given radius, can be used in the coefficients usually associated with the two-dimensional design method for free vortex flow conditions.
3. At the design blade setting angle, as the pressure loading is increased the radial velocity component also increases at a modest rate up to the point where the downstream axial component velocity in the vicinity of the blade root reaches zero. The design/analysis equations can be expected to retain their relevance in this region of operation and have also been shown to provide useful information in regions where a degree of through-flow is absent in the inboard portion of the blade span.
4. The use of linear or nearly linear distributions of the tangential (swirl) velocity ratio for arbitrary vortex flow axial fan designs as in the Mark 2 and 3 rotor designs results in practical and acceptable blade twist.
5. Arbitrary vortex flow rotor designs offer an opportunity to alleviate the critical loading conditions usually encountered on the inboard blade region of free vortex flow fans. To retain design accuracy and restrict rotor losses, it is necessary to select a swirl (pressure loading) distribution such that the calculated value of the downstream axial velocity component at the boss is greater than some agreed-upon limit. This limit is

liable to vary with fan features such as boss ratio, and at this juncture a comprehensive set of suggested limit values is unavailable. However, in the case of the lower boss ratio fans (typified by the Mark 1, 2, and 3 rotors) a minimum value for the downstream axial velocity ratio of 0.4 is tentatively suggested for design purposes.

6. The use of profile and secondary drag data based on those used in the free vortex flow design method results in acceptable estimates of rotor total efficiency corresponding to near-optimum rotor tip clearance conditions (ie, $t_c < 1\%$). However, many arbitrary vortex flow fan applications require relatively small diameter rotors, which experience rotor blade Reynolds numbers below the critical Reynolds number regime for airfoil blades with low inlet turbulence [1]. The maximum lift capability and the region of minimum profile drag in these low Reynolds number regimes is known to change significantly for many airfoils [7, 8]. The low Reynolds number data available are either incomplete or nonexistent for many of the prospective airfoils that might be considered for arbitrary vortex flow fan rotors.
7. Since the measured and predicted total pressure rises are in approximate agreement for all three blading arrangements, the design/analysis technique has general applicability and is not unique to a particular axial fan blading arrangement. Thus, cambered plate rotor blading can be designed with the same accuracy as the airfoil type.
8. The use of conservative design values of lift coefficient C_L in the blade tip region can significantly improve the fan/rotor stall performance characteristics. The reduced inboard rotor static pressure rise (typified in Fig. 7*e*) together with the radial flows that induce the inboard flow away from the hub surface are also thought to be responsible for the continuing general fan flow stability in the presence of zero inboard axial velocities downstream of the rotor. These features are responsible for the very generous margin between the design and stall conditions in respect to the Mark 2 and 3 rotors.
9. In arbitrary vortex flow rotor design, it is suggested that the blade root load limitation be based on the blade loading factor $C_L\sigma$ instead of the usual free vortex flow blade root load design criteria [1]. "Wall" stall is considered far less likely in the arbitrary vortex flow case owing to the reduction in inboard static pressure rise, whereas it is believed to be of first-order importance in the free vortex flow case. As in the Mark 2 and 3 rotor designs, this enables a significant chord reduction in the inboard blade region to be achieved, provided the associated lift coefficients are attainable after consideration has been given to the effects of multiplane blade interference. Blade chord reduction will normally be combined with modest increases in blade camber in order to meet the larger lift coefficient requirement. Most arbitrary vortex flow type fans of a high nondimensional pressure type will have the potential for a maximum solidity of approximately unity at the blade root, since the blade loading limit $C_L\sigma$ for ideal inflow conditions is approximately 1.2. With blade interference playing a relatively minor role in these instances, the resulting design lift coefficients should be readily obtained using cambered sections matched to the lift force requirements. The above design guidance on blade loading should be given provisional acceptance only at this stage.
10. In the absence of a diffuser assembly and any obstructions downstream of the fan rotor, the fan discharge losses for a direct-exhaust fan/rotor configuration can be assumed (for design/analysis purposes) to be equivalent to the integrated mean flow velocity pressure at the rotor exit plane.
11. Increasing the rotor tip clearance ratio above the preferred optimal range of $t_c = 0.5$–1% [1] has a pronounced effect on rotor performance, especially approaching the stall condition, and the performance predictions should be corrected in accordance with available experimental data.
12. The measured performance data presented for the Mark 3 rotor (Figs. 8, 9*a*, and 9*b*) indicate that the design method produces efficient rotor designs, which is one of the important prerequisites for minimizing fan noise level [1]. The present work together with Kahane's earlier work on 0.69 boss ratio rotors [2] indicates that the design/analysis technique can be used with confidence over a wide range of arbitrary vortex flow rotor boss ratios.
13. The technique appears to slightly overestimate the free-discharge and low pressure duty capabilities of an arbitrary vortex rotor in a manner similar to the midspan method proposed by Wallis [1]. However, the integrated method enables more realistic performance predictions to be obtained for the important operational region between the rotor design operating point and the onset of stall. It has previously been noted that there are no wind tunnel test data for the F-series airfoils nor any similar low Reynolds number data for the C4-series airfoils. This may, in part, account for the optimistic predictions in the free-discharge region.
14. There are, of course, other factors that limit the accuracy of the technique. The influence of wall boundary layers at the hub and duct walls, fan configuration-dependent losses, upstream turbulence and Reynolds number effects, losses associated with blade root clearance on adjustable pitch blading, and other complex radial and secondary flow regimes will all contribute a degree of uncertainty with respect to any fan/rotor performance predictions. However, the present method is seen to provide efficient and practical arbitrary vortex flow fan/rotor designs as well as reliable performance analysis predictions of adequate accuracy for engineering purposes.

PRACTICAL USEFULNESS AND SIGNIFICANCE

Design techniques that use the free vortex flow method [1] have enabled highly efficient ducted axial fan units to be developed. However, many applications exist where it may be considered impractical to mount the fan rotor in a conventional duct and/or to incorporate ancillary components such as stators and a diffuser, for example, in the case of on-road vehicle cooling systems. These arbitrary vortex flow fans are already widely used in industrial and commercial applications, with many of the installations and rotor designs being far from optimized.

The arbitrary vortex flow fan design and analysis techniques presented in this paper offer industry a reliable engineering basis for designing low to medium pressure rise rotor-only axial fans, where practical blade and fan construction considerations result in spanwise gradients of axial velocity and total pressure downstream of the rotor. The method can be used with confidence over a wide range of arbitrary vortex flow rotor boss ratios and will also enable the performance of an existing axial fan or rotor to be evaluated as a prelude to upgrading the unit's performance through rotor redesign.

CONCLUSIONS

Arbitrary vortex flow design and analysis methods for rotor-only axial flow fans (which possess spanwise gradients of both total pressure rise and downstream axial velocity) have been evaluated against the measured performance of three alternative experimental axial rotor bladings. The method is shown to predict adequately the important rotor performance characteristics of the three rotors. It is to be concluded that the equations in the Appendix, pertaining to axial rotors having either cambered plate or airfoil blading, can be used with confidence provided the design guidelines given in this paper are observed.

The design method is seen to offer industry a relatively simple and reliable engineering design tool that enables efficient and practical blading designs to be achieved for rotor-only axial fan applications. The ability to adequately predict the approximate performance of these axial fan/rotor configurations over a range of blade setting angles, rotor boss ratios, and fan loadings is important in developing new general-purpose rotor blade designs.

Well-designed arbitrary vortex flow rotor-only axial fans are efficient and quiet in operation, and exhaust efficiencies up to 60% can be achieved in direct-exhaust applications. Rotor designs featuring no blade overlap are readily achievable. This enables one-piece fixed-pitch axial fan rotors to be mass produced cheaply using injection molding technology.

APPENDIX. DESIGN EQUATIONS FOR AN ISOLATED "ARBITRARY VORTEX FLOW" AXIAL FAN ROTOR

Mass and Momentum Balance Through a Rotor Blade Row

The design equations use the mass and momentum budgets as applied to airfoil cascades. Figure A.1 depicts part of an initially cylindrical stream surface that is assumed to deviate only radially due to the influence of the moving rotor. This stream surface forms the top surface of a control volume of thickness δr (normal to the page), which is a function of position. Our frame of reference is attached to the rotor. The parameters relevant to the problem are shown in Fig. A.1*a*: the mean absolute flow velocity vectors, the mean upstream and downstream static pressures, the assumed force vector components imposed on the blade by the fluid (solid lines), and the assumed force vector components imposed on the fluid by the blade (dashed lines).

If the flow has a radial component, the control volume thickness will not be a constant, as depicted in Fig. A.1*b*.

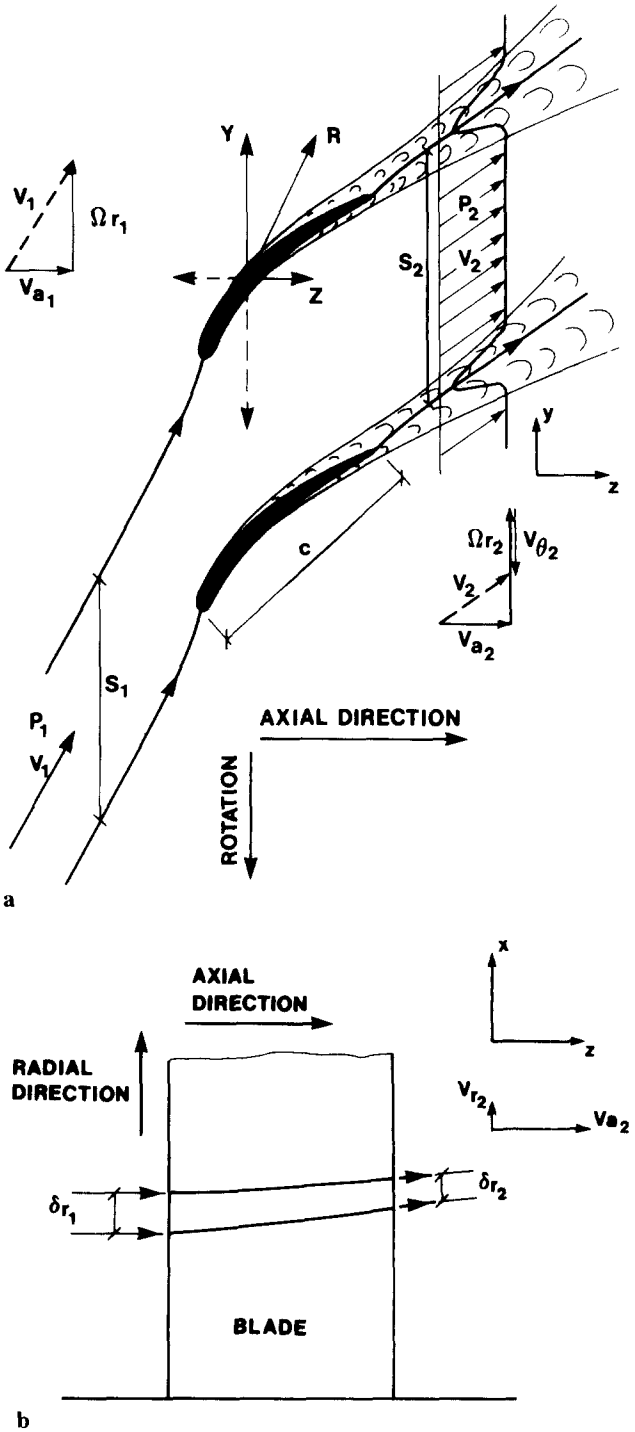

Figure A1. (*a*) Control volume for mass and momentum balance for flow through an axial fan rotor; (*b*) side view showing radial flow.

Assuming small radial movement of the streamtube, the corresponding axial and tangential momentum budgets (where the sum of external forces acting on the control volume is equated to the efflux rate of momentum from the control volume) are given approximately by

$$-\mathbf{Z} + (P_1 - P_2)\bar{s}\overline{\delta r} - \mathbf{E} = \rho \int_0^{s_2} V_{a_2}^2 \delta r_2 \, dy - \rho V_{a_1}^2 s_1 \, \delta r_1 \tag{A.1}$$

and neglecting the effect of the Coriolis force

$$-\mathbf{Y} = -\rho \int_0^{s_2} V_{a_2} V_{\theta_2}\, \delta r_2\, dy \tag{A.2}$$

The shear stress term, **E**, due to the wake flow is taken to be zero because it is assumed that the blades are well designed and the wakes are essentially symmetrical [1]. In these equations, the subscripts 1 and 2 refer to upstream and downstream of the blade row, respectively. The terms $\overline{\delta r}$ and $\bar{s}$ represent the mean radial increment and the mean control volume width, respectively, and are approximated by

$$\overline{\delta r} = (1/2)(\delta r_1 + \delta r_2) \tag{A.3a}$$

and

$$\bar{s} = (1/2)(s_1 + s_2) \tag{A.3b}$$

The mass conservation requirement is

$$s_1 V_{a_1}\, \delta r_1 = \int_0^{s_2} V_{a_2}\, \delta r_2\, dy \tag{A.4}$$

Assuming that the wake regions are small, so that there is little variation in $V_{a_2}\, \delta r_2$ in the tangential direction, allows the continuity equation to be approximated by

$$s_1 V_{a_1}\, \delta r_1 = s_2 V_{a_2}\, \delta r_2 \tag{A.5}$$

For a uniform upstream flow velocity profile, $V_{a_1} = \bar{V}_a$, and defining

$$(*) \quad \Sigma_a = \frac{V_{a_2}}{V_{a_1}} = \frac{V_{a_2}}{\bar{V}_a} = \frac{s_1\, \delta r_1}{s_2\, \delta r_2} \tag{A.6}$$

allows Eqs. (A.1) and (A.2) to be written in the form

$$\mathbf{Z} = (P_1 - P_2)\bar{s}\overline{\delta r} - \rho s_1\, \delta r_1 \bar{V}_a^2 (\Sigma_a - 1) \tag{A.7}$$

and

$$\mathbf{Y} = \rho s_1\, \delta r_1 \bar{V}_a^2 \epsilon_s \tag{A.8}$$

where the swirl coefficient is defined by

$$(*) \quad \epsilon_s = V_{\theta_2}/\bar{V}_a \tag{A.9}$$

The equations marked with (*) are of central importance to the arbitrary vortex flow rotor design and analysis calculations. It should be noted that it has been assumed that there is no preswirl. The equations that include the effects of preswirl can be derived in a similar manner. Also note that for the momentum balance equation in the radial direction, the effect of centrifugal force must be considered. An approximate radial equilibrium equation is derived in a later section.

Mean Flow Velocity Vector Across the Rotor Blade Row

The mean flow velocity across the blade row is an important parameter in determining the lift and drag blade force components. Referring to Figs. A.1*b* and A.2, the mean flow velocity across an airfoil rotor blade with no preswirl but with radial flow present is given by

$$\bar{V}_m^2 = \left(\frac{V_{a_1} + V_{a_2}}{2}\right)^2 + \left(\frac{2\Omega\bar{r} - V_{\theta_2}}{2}\right)^2 + \bar{V}_r^2 \tag{A.10}$$

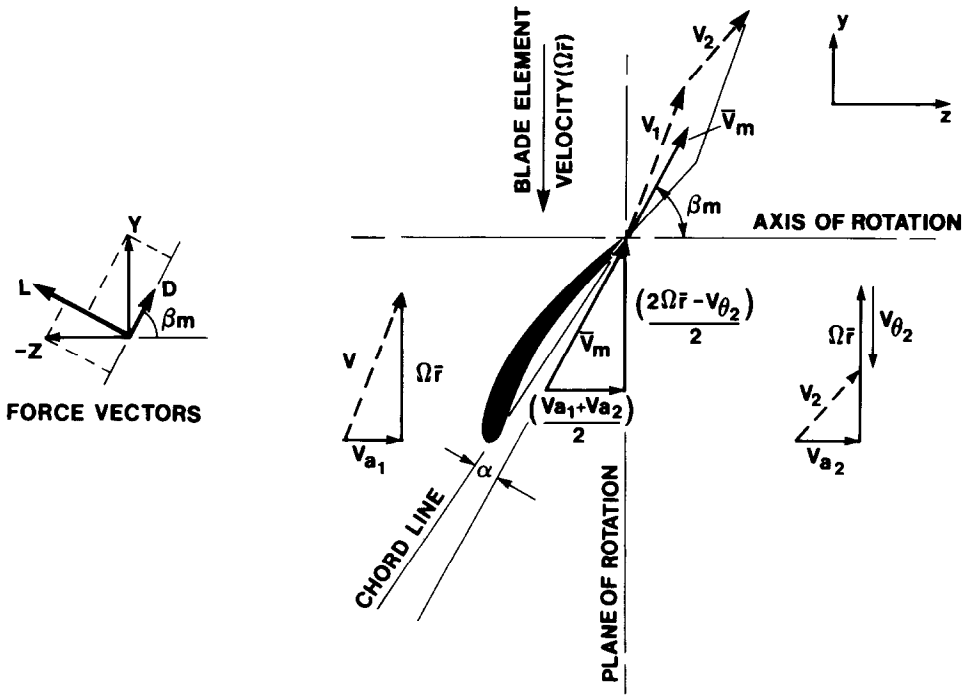

Figure 2. Relative velocity vectors across the rotating blade element and assumed force vector components imposed on the blade element resulting from the flow.

or

$$\frac{\bar{V}_m^2}{\bar{V}_a^2} = \frac{1}{4}\left(1 + \frac{V_{a_2}}{\bar{V}_a}\right)^2 + \left[\frac{\Omega\bar{r}}{\bar{V}_a} - \left(\frac{1}{2}\right)\frac{V_{\theta_2}}{\bar{V}_a}\right]^2 + \frac{\bar{V}_r^2}{\bar{V}_a^2} \tag{A.11}$$

Neglecting the second-order effects due to radial flow gives

$$\frac{\bar{V}_m^2}{\bar{V}_a^2} = \frac{1}{4}(1 + \Sigma_a)^2 + \left(\frac{1}{\lambda} - \frac{1}{2}\epsilon_s\right)^2 \tag{A.12}$$

In this equation the local flow coefficient λ is defined by $\lambda = \bar{V}_a/\Omega\bar{r}$.

The following trigonometric properties are also useful:

$$\tan\beta_m = \frac{\Omega r - (1/2)V_{\theta_2}}{(1/2)(V_{a_1} + V_{a_2})} = \frac{\Omega r/\bar{V}_a - (1/2)V_{\theta_2}/\bar{V}_a}{(1/2)(1 + \Sigma_a)}$$

$$(*)\quad \tan\beta_m = 1/\lambda' - (1/2)\epsilon_s' \tag{A.13}$$

where the modified local flow and swirl coefficients have been defined as

$$(*)\quad \lambda' = (1/2)(1 + \Sigma_a)\lambda \tag{A.14a}$$

and

$$(*)\quad \epsilon_s' = 2\epsilon_s/(1 + \Sigma_a) \tag{A.14b}$$

Also,

$$\cos\beta_m = \frac{1}{2}\left(\frac{V_{a_1} + V_{a_2}}{\bar{V}_m}\right) = \frac{1}{2}\left(\frac{1 + \Sigma_a}{\bar{V}_m/\bar{V}_a}\right) \tag{A.15}$$

Thus the nondimensional mean flow velocity over a blade section is given by

$$\frac{\bar{V}_m}{\bar{V}_a} = \frac{1}{2}\left(\frac{1 + \Sigma_a}{\cos\beta_m}\right) \tag{A.16}$$

Lift and Drag Coefficients

The drag coefficient C_D is defined by

$$\mathbf{D} = C_D(1/2)\rho\bar{V}_m^2 c\,\delta r \tag{A.17}$$

If radial flow occurs, this equation must be written as

$$\mathbf{D} = C_D'(1/2)\rho\bar{V}_m^2 c'\,\overline{\delta r} \tag{A.18}$$

where C_D' is different from C_D because the radial flow effectively means that the blade chord and the shape of the airfoil will be different.

The new chord (c') can be expressed as

$$c' = c\left[1 + \frac{1}{2}\left(\frac{\bar{V}_r}{\bar{V}_m}\right)^2 + \cdots\right] \tag{A.19}$$

If second-order effects due to radial flow are neglected, Eq. (A.18) becomes

$$\mathbf{D} = C_D(1/2)\rho\bar{V}_m^2 c\,\overline{\delta r} \tag{A.20}$$

A similar analysis for the lift coefficient yields

$$\mathbf{L} = C_L(1/2)\rho\bar{V}_m^2 c\,\overline{\delta r} \tag{A.21}$$

Resolving the Lift and Drag Coefficients for a Rotor Blade

Referring to Fig. A.2, the lift and drag forces on the airfoil blade element can be expressed in terms of the force components **Y** and **Z** imposed by the flow:

$$\mathbf{D} = +\mathbf{Z}\cos\beta_m + \mathbf{Y}\sin\beta_m \tag{A.22a}$$

$$\mathbf{L} = -\mathbf{Z}\sin\beta_m + \mathbf{Y}\cos\beta_m \tag{A.22b}$$

Rearranging Eq. (A.22a) gives

$$\mathbf{Z} = \frac{+\mathbf{D} - \mathbf{Y}\sin\beta_m}{\cos\beta_m} \tag{A.23}$$

which allows Eq. (A.22b) to be written

$$\mathbf{L} = -\mathbf{D}\tan\beta_m + \frac{\mathbf{Y}}{\cos\beta_m} \tag{A.24}$$

Substituting for **L**, **D**, and **Y** from Eqs. (A.21), (A.20), and (A.8) and noting that $s_1\,\delta r_1\bar{V}_a \simeq \bar{s}\overline{\delta r}(\bar{V}_a + V_{a_2})/2$ allows the lift coefficient to be expressed as

$$C_L = -C_D\tan\beta_m + \frac{\rho s_1\,\delta r_1\bar{V}_a^2\epsilon_s}{\cos\beta_m(1/2)\rho\bar{V}_m^2 c\,\overline{\delta r}} = -C_D\tan\beta_m + \frac{(1/2)\rho\bar{s}\overline{\delta r}(1 + \Sigma_a)\bar{V}_a^2(1/2)\epsilon_s'(1 + \Sigma_a)}{\cos\beta_m(1/2)\rho\bar{V}_m^2 c\,\overline{\delta r}} \tag{A.25}$$

which, after substituting from Eq. (A.16), yields

$$(*)\quad C_L = -C_D\tan\beta_m + (2\epsilon_s'/\sigma)\cos\beta_m \tag{A.26}$$

where $\sigma = c/\bar{s}$ is the blade solidity.

The blade loading factor $C_L\sigma$ [1] is then given by

$$(*)\quad C_L\sigma = -C_D\sigma\tan\beta_m + 2\epsilon_s'\cos\beta_m \tag{A.27}$$

Pressure Relationships Across a Rotor Blade Row

The total pressures before and after passing through a rotor blade element are given by

$$H_1 = P_1 + (1/2)\rho V_{a_1}^2 \tag{A.28a}$$

and

$$H_2 = P_2 + (1/2)\rho\left(V_{a_2}^2 + V_{\theta_2}^2 + V_{r_2}^2\right) \tag{A.28b}$$

The rate of work (δW) done by a rotor blade element is

given by the product of the volume flow rate and the total pressure rise across the blade element.

$$\delta W = 2\pi r_1 \, \delta r_1 \bar{V}_a \, \Delta h_{\text{th}} \tag{A.29}$$

where Δh_{th} is the theoretical maximum pressure rise on passing through the blade element section and is given by

$$\Delta h_{\text{th}} = H_2 - H_1 + \Delta h_R \tag{A.30}$$

The term Δh_R represents the losses across the rotor blade element.

The elemental torque (δT) on a blade element with no preswirl present is given by the product of the mass flow rate and the angular velocity change through the blade element,

$$\delta T = 2\pi r_1 \, \delta r_1 \bar{V}_a \, \rho(V_{\theta_2} r_2) \tag{A.31}$$

Equating the rotor shaft power input $\Omega \, \delta T$ to the rate of work done by the blade element,

$$\Omega 2\pi r_1 \, \delta r_1 \bar{V}_a \, \rho(V_{\theta_2} r_2) = 2\pi r_1 \, \delta r_1 \bar{V}_a \, \Delta h_{\text{th}}$$

gives

$$\Delta h_{\text{th}} = \Omega \rho V_{\theta_2} r_2 \tag{A.32}$$

A nondimensional theoretical local total pressure rise coefficient can be defined as

$$(*) \quad k_{\text{th}} = \frac{\Delta h_{\text{th}}}{(1/2)\rho \bar{V}_a^2} = 2\epsilon_s \frac{1}{\lambda_{r_2}} \tag{A.33}$$

It is also useful to define a nondimensional local static pressure rise as

$$\frac{P_2 - P_1}{(1/2)\rho \bar{V}_a^2} = k_{\text{th}} - k_R - \epsilon_s^2 - \Sigma_r^2 + (1 - \Sigma_a^2) \tag{A.34}$$

Neglecting the second-order effects due to radial flow gives

$$(*) \quad \frac{P_2 - P_1}{(1/2)\rho \bar{V}_a^2} = k_{\text{th}} - k_R - \epsilon_s^2 + (1 - \Sigma_a^2) \tag{A.35}$$

Lift Coefficients from Rotor Blade Elements

Lift and drag force data for C4-series airfoils, flat undersurface airfoils, and elliptical airfoils and for cambered plates are summarized in Ref. 1.

Lift coefficient data for isolated C4 airfoils (corresponding to Re = 3.2×10^5–6.4×10^5) are given in Ref. 17 and Fig. 6.6 of Ref. 1. A tabulation based on the data given in Ref. 17 (corresponding to Re = 3.2×10^5) has been used in this instance to calculate approximate lift coefficient data for F-series airfoils (C4-series airfoils with leading edge droop) as a function of camber angle θ between 0 and 8% and angle of incidence α_{0d} between $-4°$ and $+16°$, where α_{0d} is the angle of incidence to the circular arc camber line of an airfoil that may also have leading edge nose droop [1]. The incidence angle with respect to the F-series airfoil chord line is given by

$$\alpha = \alpha_{0d} - 0.57d \tag{A.36}$$

Lift coefficient data for 2% thick cambered plates (corresponding to Re = 3×10^5–6×10^5) are given in Figs. 6.22–6.24 of Ref. 1. A tabulation based on the data given in Fig. 6.22 of Ref. 1 (corresponding to Re = 3×10^5) has been used in this instance to calculate the lift coefficient as a function of camber angle θ between 0 and 8% and angle of incidence α between $-4°$ and $+16°$.

Reynolds number effects and blade surface irregularities can also significantly modify an airfoil's lift and drag performance, and further design guidance is available in Fig. 6.10 and Section 10.2.2 of Ref. 1. However, thin cambered plate blades are reported to be far less sensitive to Reynolds number effects [1].

Drag Coefficients for a Rotor Blade Row

It is convenient to approximate the drag coefficient for an axial fan rotor blade row by the sum of two components, C_{D_P}, the profile drag associated with flow over a blade section, and C_{D_S}, the blading secondary drag (based on the midspan blade element), which includes all other rotor/blade losses, such as wall boundary layer losses, blade tip clearance flow, and end wall friction.

Profile drag data for C4-series airfoils are given in Ref. 17 and Fig. 6.11 of Ref. 1. A tabulation based on the data given in Ref. 17 (corresponding to Re = 3.2×10^5) has been used in this instance to calculate C_{D_P} data for F-series airfoils (C4-series airfoils with leading edge droop) as a function of lift coefficient and the blade camber for each blade element. The value of C_{D_P} was further modified for Reynolds number and for the influence of rotor blade solidity using the data shown in Fig. 6.10 of Ref. 1.

Profile drag data for 2% thick cambered plates, as given in Fig. 6.28 of Ref. 1 (corresponding to Re = 3.2×10^5), can be tabulated similarly. However, Reynolds number and solidity adjustments in this case are considered unwarranted, with Reynolds number having only a minor influence on lift and drag properties of thin, constant-thickness cambered plates [1].

Existing data on fan secondary drag losses suggest that there is an approximately quadratic dependence on the lift coefficient at the midspan blade element, and the following equation was tentatively suggested as being adequate for axial rotor design purposes [1]:

$$C_{D_S} = bC_{L_{\text{midspan}}}^2 \tag{A.37}$$

where b is an undefined function of blade aspect ratio, Reynolds number, and blade stagger angle.

In the present instance it has been found that combining an annulus drag component with the secondary drag estimate [1] improves the agreement between the measured and predicted rotor performance and provides conservative rather than optimistic estimates of rotor efficiency and power consumption. The following equation has been adopted for estimating these latter drag components:

$$C_{D_S} = bC_{L_{\text{midspan}}}^2 + 0.02c/\sigma l \tag{A.38}$$

For cambered plate blades a suggested value for the coefficient b is approximately 0.025 [1], and for conventional fan airfoils such as the F-series [6], a suggested value for b is approximately 0.018 [1].

Multiplane Interference Factor for Airfoils

When the blade solidity is high, the two-dimensional lift and drag coefficients need to be modified to account for

an interference effect by neighboring rotor blades. This interference effect manifests itself by modifying the lift curve slope and drag performance of the airfoil [1]. An interference factor C_L/C_{L_i} [1] is employed in adjusting the angle of incidence of the blade section to correspond to C_{L_i}, it being assumed that the no-lift angle of the blade section remains unchanged with blade proximity. The multiplane interference effect is expressed in terms of the ratio of the lift coefficient C_L achieved by the rotor blade element to the lift coefficient C_{L_i} achieved by the same airfoil element in isolation from other airfoils and is dependent on stagger angle and blade solidity (as shown in Fig. 6.29 of Ref. 1). These data have been tabulated and used in the calculations performed for this paper.

Rotor Losses Across a Rotor Blade Row

From Eqs. (A.22a) and (A.20), we can write the drag coefficient as

$$C_D = \frac{1}{(1/2)\rho \bar{V}_m^2 c \overline{\delta r}} (\mathbf{Z} \cos \beta_m + \mathbf{Y} \sin \beta_m) \quad \text{(A.39)}$$

Substituting Eqs. (A.7) and (A.8) for **Z** and **Y** gives

$$C_D = \frac{1}{(1/2)\rho \bar{V}_m^2 c \overline{\delta r}} \Big\{ + \Big[(P_1 - P_2) \bar{s} \overline{\delta r} - \rho s_1 \, \delta r_1 \bar{V}_a^2 (\Sigma_a - 1) \Big] \cos \beta_m + \Big[\rho s_1 \, \delta r_1 \bar{V}_a^2 \epsilon_s \Big] \sin \beta_m \Big\} \quad \text{(A.40)}$$

and using Eq. (A.14b), this becomes

$$C_D = \frac{1}{(1/2)\rho \bar{V}_m^2 c \, \overline{\delta r}} \left\{ + \left[(P_1 - P_2) \bar{s} \, \overline{\delta r} - \frac{1}{2}(1 + \Sigma_a) \overline{\delta r} \rho \bar{s} \bar{V}_a^2 (\Sigma_a - 1) \right] \cos \beta_m + \left[\frac{1}{2}(1 + \Sigma_a) \overline{\delta r} \rho \bar{s} \bar{V}_a^2 \epsilon_s' \frac{1}{2}(1 + \Sigma_a) \right] \sin \beta_m \right\} \quad \text{(A.41)}$$

which, using Eq. (A.16), simplifies to

$$C_D = \frac{4 \cos^2 \beta_m}{\sigma (1 + \Sigma_a)^2} \times \left\{ - \left[\frac{1}{(1/2)\rho \bar{V}_a^2} (P_2 - P_1) - (1 - \Sigma_a^2) \right] \cos \beta_m + \frac{1}{2}(1 + \Sigma_a)^2 \epsilon_s' \sin \beta_m \right\} \quad \text{(A.42)}$$

Then, using Eqs. (A.34), (A.33), and (A.13) and neglecting second-order radial velocity terms allows Eq. (A.42) to be written as

$$C_D = \frac{4 \cos^3 \beta_m}{\sigma (1 + \Sigma_a)^2} \left[- \left(2 \epsilon_s \frac{1}{\lambda_{r_2}} - k_R - \epsilon_s^2 \right) + \frac{1}{2}(1 + \Sigma_a)^2 \epsilon_s' \left(\frac{1}{\lambda'} - \frac{1}{2} \epsilon_s' \right) \right] \quad \text{(A.43)}$$

Finally, using Eqs. (A.14a) and (A.14b) and rearranging allows the blade element losses to be estimated:

$$(*) \quad k_R = \frac{\sigma (1 + \Sigma_a)^2}{4 \cos^3 \beta_m} C_D \quad \text{(A.44)}$$

The actual local rotor total pressure rise coefficient (including downstream swirl) is defined as

$$(*) \quad k_r = k_{\text{th}} - k_R \quad \text{(A.45)}$$

The rotor blade element efficiency estimate (the ratio of the actual rotor total pressure rise to the theoretical rotor total pressure rise) is given by

$$(*) \quad \eta_{Rb} = k_r / k_{\text{th}} \quad \text{(A.46)}$$

Radial Equilibrium Equation for a Blade Row with No Preswirl

Assuming that the radial velocity component is small, an equation can be derived for the downstream axial velocity in terms of the swirl coefficient.

From Eqs. (A.30) and (A.32), the theoretical total pressure rise on passing through the rotor blade element is related to the swirl through

$$\Delta h_{\text{th}} = H_2 - H_1 + \Delta h_R = \frac{H_2 - H_1}{\eta_{Rb}} = \rho V_{\theta_2} r_2 \Omega \quad \text{(A.47)}$$

Hence,

$$H_2 - H_1 = \eta_{Rb} \rho V_{\theta_2} r_2 \Omega \quad \text{(A.48)}$$

Also, from Eqs. (A.28a) and (A.28b) and neglecting second-order radial velocity terms,

$$H_2 - H_1 = P_2 - P_1 + (1/2)\rho \left(V_{a_2}^2 + V_{\theta_2}^2 - V_{a_1}^2 \right) \quad \text{(A.49)}$$

Combining these two expressions and simplifying gives

$$\frac{2 \epsilon_s \eta_{Rb}}{\lambda_{r_2}} = \frac{P_2 - P_1}{(1/2)\rho \bar{V}_a^2} + \epsilon_s^2 + \Sigma_a^2 - 1 \quad \text{(A.50)}$$

Now assuming that the radial pressure gradient upstream is zero since there is no preswirl and that equilibrium downstream is reached quickly, the radial pressure gradient must balance the centrifugal force. This implies that

$$\frac{1}{\rho} \frac{dP}{dr} = \frac{V_{\theta_2}^2}{r} \quad \text{(A.51)}$$

If the radius ratio is defined as

$$x = r/R \quad \text{(A.52)}$$

then integrating gives

$$P_2 - P_{2_{x_0}} = \rho \int_{x_0}^{x} \frac{V_{\theta_2}^2}{x} \, dx \quad \text{(A.53)}$$

where x_0 is an arbitrary radial position. This can be further reduced to

$$\frac{P_2 - P_{2_{x0}}}{(1/2)\rho \bar{V}_a^2} = 2\int_{x_0}^{x} \frac{\epsilon_s^2}{x}\, dx \qquad \text{(A.54)}$$

Finally, combining Eqs. (A.54) and (A.50) yields

$$(*)\quad 2\epsilon_s \eta_{Rb}\frac{1}{\lambda} - \epsilon_s^2 - \Sigma_a^2 = \left[2\epsilon_s \eta_{Rb}\frac{1}{\lambda} - \epsilon_s^2 - \Sigma_a^2\right]_{x_0} + 2\int_{x_0}^{x} \frac{\epsilon_s^2}{x}\, dx \qquad \text{(A.55)}$$

This equation can be solved to give the downstream axial velocity coefficient provided the swirl distribution is given. The usual approach is to take x_0 to be the position where $\Sigma_a = 1$; Σ_a is then given explicitly provided x_0 is known. In this regard, the downstream axial velocity component must satisfy the global mass conservation condition

$$(*)\quad \frac{2}{1 - x_b^2}\int_{x_b}^{1} \Sigma_a x\, dx = 1 \qquad \text{(A.56)}$$

Thus x_0 can be adjusted until Eq. (A.56) is satisfied. Once Σ_a is calculated, the radial flow can be estimated from continuity requirements by integrating the upstream and downstream flow with respect to radius.

Tip Clearance Effects for a Rotor Blade Row Rotating in a Fan Duct

Figure 10 indicates that the performance penalties associated with increasing blade tip clearance on the Mark 3 fan/rotor are minimal during "free-discharge" and low pressure duty operation but become quite significant at higher pressure duties and must be taken into account when attempting to predict the performance of the rotor in an actual fan configuration.

The decrement in fan inlet total pressure capability (Fig. 11) was determined along assumed quadratic system resistance curves shown in Fig. 10. These data have been incorporated in the Mark 3 fan/rotor performance predictions for the range of blade setting angles presented in this paper.

NOMENCLATURE

- b coefficient (undefined function of blade aspect ratio, Re, and ξ) sed in an approximate expression for C_{D_S} [1], dimensionless
- C_D drag coefficient ($= C_{D_P} + C_{D_S}$) for a fan blade element with respect to $\bar{V}_m$, dimensionless
- C_D' drag coefficient for the radial flow case, dimensionless
- C_{D_P} profile drag coefficient for a blade element, dimensionless
- C_{D_S} secondary drag coefficient based on the blade midspan element, Eq. (A.38), dimensionless
- C_L lift coefficient for a blade element with respect to $\bar{V}_m$, dimensionless
- C_{L_i} isolated airfoil lift coefficient, dimensionless
- c local blade element chord length, Fig. 1; the length of a chord line that passes through the blade surface intercept points of the blade camber line at or near the leading and trailing edges of the blade, m
- c' equivalent local blade element chord for the radial flow case, m
- D diameter of fan duct, m
- **D** drag force on the blade element, Fig. A.2, N
- d F-series airfoil nose droop expressed as a percentage of chord [1, 6], %
- **E** a shear stress term due to the wake flow [1], N
- FITP fan inlet total pressure ($= -$ITP), for exhaust fans [1, 5], Pa
- FTP fan total pressure (= OTP − ITP), for inline and blower fans [1, 5], Pa
- H_1 local total pressure in the fan annulus upstream of a rotor blade element, Pa
- H_2 local total pressure in the fan annulus downstream of a rotor blade element, Pa
- ΔH_r rotor mean total pressure rise, including downstream swirl component, Pa
- ΔH_{th} theoretical rotor mean total pressure rise, including downstream swirl component [$= \Delta H_r/(\eta_{Rb}/100)$ [1], FTP$/(\eta_T/100)$, FITP$/(\eta_E/100)$], Pa
- Δh_R local total pressure loss across a blade element, Pa
- Δh_{th} theoretical local total pressure rise across a blade element, Eq. (A.30), Pa
- ITP mean inlet total pressure to a fan unit [1, 5], Pa
- K_{th} theoretical rotor mean total pressure rise coefficient [1] [$= \Delta H_{\text{th}}/((1/2)\rho \bar{V}_a^2)$], dimensionless
- k_R local total pressure loss coefficient across a blade element, Eq. (A.44), dimensionless
- k_r local total pressure rise coefficient across a blade element, Eq. (A.45), dimensionless
- k_{th} theoretical local total pressure rise coefficient across a blade element, Eq. (A.33), dimensionless
- **L** lift force on the blade element, Fig. A.2, N
- l blade length, m
- N impeller shaft rotational speed,† rev/s
- n number of equally spaced fan blades on the rotor, dimensionless
- OTP mean outlet total pressure from a fan unit [1, 5], Pa
- P local static pressure, Pa
- P_1 local static pressure upstream of a rotor blade element in the fan annulus, Pa
- P_2 local static pressure downstream of a rotor blade element in the fan annulus, Pa
- Δp_r local static pressure rise across a blade element, Pa
- Q fan inlet volume flow rate, m^3/s
- R radius of fan duct, m
- **R** blade element reaction force, Fig. A.1*a*, N
- Re approximate blade chord Reynolds number [5] ($= \Omega R c \rho/\mu$), dimensionless
- r radius corresponding to rotor blade section element, m
- r_1 radius corresponding to rotor blade section element at inlet to blade, m

† for convenience the rotational speed is expressed in revolutions per minute, rpm, throughout the general text and figures.

r_2 radius corresponding to rotor blade section element at outlet from blade, m
r_b radius of rotor boss or hub, m
r_t radius of rotor blade tip, m
$\bar{r}$ mean radius of blade element from rotor shaft centerline, m
δr radial spanwise blade element increment for the no radial flow case, m
δr_1 radial increment corresponding to blade element at radius r_1, m
δr_2 radial increment corresponding to blade element at radius r_2, m
$\overline{\delta_r}$ mean radial increment as defined in Eq. (A.3*a*), m
s_1 circumferential spacing at radius r_1 of adjacent rotor blades, m
s_2 circumferential spacing at radius r_2 of adjacent rotor blades, m
$\bar{s}$ mean control volume width as defined in Eq. (A.3*b*), m
δT blade element torque about rotor shaft axis, N · m
t cambered plate blade thickness, m
t_c rotor blade tip clearance ratio [$= 100(R - r_t)/R(R - r_b)$], %
V_1 upstream local air velocity vector relative to the blade, m/s
V_2 downstream local air velocity vector relative to the blade, m/s
$\bar{V}_a$ mean axial velocity based on fan inlet volume flow rate and fan annulus duct cross-sectional area, m/s
V_{a_1} upstream local axial velocity component in the fan annulus, m/s
V_{a_2} downstream local axial velocity component in the fan annulus, m/s
$\bar{V}_m$ mean local air velocity vector relative to the blade element for the no preswirl flow case, Fig. A.2, m/s
$\bar{V}_r$ mean local radial velocity component, m/s
V_{r_2} downstream local radial velocity component in the fan annulus, m/s
V_{θ_2} downstream local tangential velocity component in the fan annulus, m/s
W rotor shaft input power, W
δW rate of work done by a blade element, W
x radius ratio; defined by $x = r/R$, dimensionless
x_b rotor boss or hub radius ratio; defined by $x_b = r_b/R$, dimensionless
x_0 arbitrary nondimensional radial position, dimensionless
Y reaction force component in the tangential direction imposed by the flow on the blade element, Fig. A.1*a*, N
Z reaction force component in the axial direction imposed by the flow on the blade element, Fig. A.1*a*, N

Greek Symbols

α incidence angle between $\bar{V}_m$ and the airfoil chord line, Fig. A.2, deg
α_{0d} incidence angle between the mean velocity $\bar{V}_m$ and the circular arc chord line of an F-series airfoil with no additional leading edge camber [1, 6], deg
$\Delta\alpha_d$ angle between the airfoil chord line and circular arc chord line in an F-series airfoil with additional leading edge camber [1, 6], Fig. 1 (= 0.57*d*), deg
β_m angle between mean velocity $\bar{V}_m$ and the axis of rotation, Fig. A.2, deg
ϵ_s local swirl coefficient [1], as defined in Eq. (A.9), dimensionless
ϵ_s' modified local swirl coefficient [1], as defined in Eq. (A.14*b*); dimensionless
η_E fan efficiency, exhaust [5] {= 100[Q(FITP)/W]}, %
η_R rotor efficiency, total [= 100($Q\Delta H_r/W$)], %
η_{Rb} rotor blade element efficiency total, as defined in Eq. (A.46), %
η_T fan efficiency, total [5] {= 100[Q(FTP)/W]}, %
θ blade camber angle, Fig. 1; based on the circular arc camber line in the case of an F-series airfoil, deg
Λ rotor tip flow coefficient [1] ($= \bar{V}_a/\Omega R$), dimensionless
λ local rotor flow coefficient at blade element radius r [1] ($= \bar{V}_a/\Omega r$), dimensionless
λ' modified local flow coefficient as defined in Eq. (A.14*a*), dimensionless
μ air viscosity, Pa · s
ξ rotor local blade element stagger angle, the angle between an airfoil blade element chord line and the axis of rotation, Fig. 1 ($= \beta_m - \alpha$), deg
ρ air density, kg/m^3
Σ_a axial velocity ratio as defined in Eq. (A.6), dimensionless
Σ_r radial velocity ratio ($= V_{r_2}/\bar{V}_a$), dimensionless
σ solidity of the blading [1] ($= c/\bar{s}$), dimensionless
Φ fan volume flow rate coefficient [5] Φ ($= Q/ND^3$), dimensionless
ϕ_p practical blade setting angle, Fig. 1; the angle between the plane of rotation and a line passing through the two contact points when the under-surface of an airfoil blade element is contacted with a straight edge, deg
ϕ_t theoretical blade setting angle, Fig. 1; the angle between the plane of rotation and an airfoil blade chord line, deg
ψ_R rotor total pressure coefficient ($= \Delta H_r/\rho N^2 D^2$), dimensionless
ψ_T fan total pressure coefficient [5] (= FTP/$\rho N^2 D^2$), dimensionless
ψ_E fan inlet total pressure coefficient [5] (= FITP/$\rho N^2 D^2$), dimensionless
$\psi_{E_{0.5}}$ fan inlet total pressure coefficient corresponding to $t_c = 0.5\%$, dimensionless
$\Delta\psi_{E_{t_c}}$ fan inlet total pressure loss coefficient [$= (\psi_{E_{0.5}} - \psi_E)/\psi_{E_{0.5}}$], dimensionless
Ω angular velocity of rotor ($= 2\pi N$), rad/s

REFERENCES

1. Wallis, R. A., *Axial Flow Fans and Ducts*, Wiley, New York, 1983.
2. Kahane, A., Investigation of Axial Flow Fan and Compressor Rotors Designed for Three-Dimensional Flow, NACA Tech. Note 1652, 1948.
3. Wallis, R. A., *Axial Flow Fans, Design and Practice*, George Newnes, London, 1961.
4. McNally, W. D., and Sockol, P. M., Review—Computational Methods for Internal Flows with Emphasis on Turbomachinery, *J. Fluids Eng., Trans. ASME*, **107**, 6–22, March 1985.

5. Australian Standard AS 2936-1987, SAA Fan Test Code, Industrial Fans—Determination of Performance Characteristics, SAA, Sydney, 1987.
6. Wallis, R. A., The F-series Aerofoils for Fan Blade Sections, *Mech. Eng. Trans., I.E. Aust.*, **ME2**(1), 12–20, 1977.
7. Miley, S. J., A Catalog of Low Reynolds Number Airfoil Data for Wind Turbine Applications, Dept. Aerospace Eng., Texas A and M, Texas, February 1982. (Subcontract No. PFY12781-W; part of U.S. Dept. of Energy Contract No. DE-AC04-76DP03533.)
8. Selig, M. S., Donovan, J. F., and Fraser, D. B., *Airfoils at Low Speeds—Soartech 8*, H. A. Stokely, Virginia Beach, Virginia, 1989.
9. Liversey, J. L., and Hugh, T., "Suitable Mean Values" in One-Dimensional Gas Dynamics, *J. Mech. Eng. Sci.*, **8**(4), 374–383, 1966.
10. Press, W. H., Flannery, B. P., Teukolsky, S. A., and Vetterling, W. T., *Numerical Recipes: The Art of Scientific Computing*, Cambridge Univ. Press, Cambridge, 1986.
11. British Standard BS 848: Part 1: 1980, Fans for General Purposes: Part 1. Methods of Testing Performance, BSI, London, 1980.
12. Loehrke, R. I., and Nagib, H. M., Control of Free-Stream Turbulence by Means of Honeycombs: A Balance Between Suppression and Generation, *J. Fluids Eng., Trans. ASME*, **981**, Ser. 1, 3, 342–353, 1976.
13. American National Standard ANSI/ASHRAE 51-1987, Laboratory Methods of Testing Fans for Rating, 1987.
14. Shepherd, I. C., A Four Hole Pressure Probe for Fluid Flow Measurements in Three Dimensions, *J. Fluids Eng., Trans. ASME*, **103**, 590–594, December 1981.
15. British Standard BS 1042: Section 1.1: 1981, Methods of Measurement of Fluid Flow in Closed Conduits, BSI, London, 1981.
16. Kline, S. J., and McClintock, F. A., Describing Uncertainties in Single Sample Experiments, *Mech. Eng.*, **75**, 3–8, January 1953.
17. Ruglen, R., Low Speed Wind Tunnel Tests on a Series of C4 Section Aerofoils. Australian Defence Scientific Service, Aeronautical Research Laboratories Aerodynamics Note 275, July 1966.

Received November 16, 1989; revised December 22, 1992